UNIVERSIDAD DEL VALLE

ANÁLISIS DE LAS FASES CUADRUPOLARES DE UN SISTEMA DE ESPÍN-1 A PARTIR DE UN ANSATZ BASADO EN REDES TENSORIALES

TENSOR NETWORK BASED ANSATZ FOR THE ANALYSIS OF A SPIN-1 SYSTEM QUADRUPOLAR PHASES

PRESENTADO POR:

ANA MARIA ENRIQUEZ ZAMUDIO

DIRIGIDO POR:

DR. RER. NAT. KAREN RODRIGUEZ RAMIREZ

FACULTAD DE CIENCIAS NATURALES Y EXACTAS

DEPARTAMENTO DE FÍSICA - 3146

SANTIAGO DE CALI, 2024

Resumen

La precisión alcanzada por las técnicas experimentales con átomos ultrafríos ha permitido la creación de simuladores cuánticos, facilitando la exploración de sistemas unidimensionales en el laboratorio. En estos sistemas, las fluctuaciones son inherentemente colectivas y se propagan a grandes distancias debido a las frecuentes colisiones. Como resultado, se han desarrollado marcos teóricos que aprovechan estas fluctuaciones para describir dichos sistemas. Los gases ultrafríos confinados en redes ópticas no solo sirven como simuladores cuánticos de sistemas tradicionales de materia condensada, sino que también actúan como plataformas para crear nuevos sistemas cuánticos de muchos cuerpos. En este trabajo, se proponen dos técnicas numéricas para explorar un gas bosónico de espín-1 contenido en una red óptica unidimensional, en la fase fuertemente interactuante y en el régimen del aislante de Mott. La primera técnica es un enfoque de campo medio, conocido como el ansatz de Gutzwiller, que aproxima la función de onda de muchos cuerpos como el producto de contribuciones individuales en cada sitio. Adicionalmente, se ha desarrollado un ansatz más avanzado que considera parejas de sitios acoplados, lo que permite explorar regiones del espacio de fases que no son accesibles con el ansatz tradicional. La segunda técnica se basa en redes tensoriales, específicamente en la representación del estado como un estado de producto de matrices (MPS), combinado con el algoritmo de Decimación en Bloques con Evolución Temporal (TEBD). Esta técnica se utiliza para analizar las propiedades del estado fundamental y el comportamiento magnético del sistema bajo la influencia de un campo magnético externo. Ambas técnicas se evaluaron en el contexto de un Hamiltoniano de Heisenberg Bilineal Bicuadrático, incorporando correcciones perturbativas para tener en cuenta el efecto Zeeman cuadrático. Los resultados de este trabajo demuestran que las redes tensoriales, en particular los MPS, proporcionan una técnica numérica robusta para capturar los fenómenos cuánticos exhibidos por los bosones de espín 1. Los cálculos de la energía del estado fundamental y los perfiles de magnetización confirman la eficacia de las redes tensoriales para representar la física esencial del sistema. Además, la investigación de las propiedades de entrelazamiento revela que la entropía de entrelazamiento del sistema sigue una ley de área, característica de los sistemas unidimensionales con gap. También se exploraron observables de quiralidad y correlación de espín, revelando información relevante sobre el comportamiento del sistema bajo diversos parámetros de interacción. Los resultados son consistentes con estudios teóricos y numéricos previos, destacando el potencial de las redes tensoriales para abordar retos en la física cuántica de muchos cuerpos. Este trabajo introduce una perspectiva numérica novedosa dentro del contexto de la investigación en Estado Sólido en la Universidad del Valle, allanando el camino para futuros estudios utilizando técnicas avanzadas de redes tensoriales.

Palabras clave: Redes tensoriales, MPS, simuladores cuánticos, Aislante de Mott, ansatz de Gutzwiller.

Abstract

The precision achieved by experimental techniques with ultracold atoms has enabled the creation of quantum simulators, facilitating the exploration of one-dimensional systems in the laboratory. In these systems, fluctuations are inherently collective and propagate over large distances due to frequent collisions. As a result, theoretical frameworks have been developed that leverage these fluctuations to describe such systems. Ultracold gases confined in optical lattices not only serve as quantum simulators for traditional condensed matter systems but also act as platforms to create new many-body quantum systems. In this work, two numerical techniques are proposed to explore a spin-1 bosonic gas contained in a one-dimensional optical lattice, in the strongly interacting phase and in the Mott insulator regime. The first technique is a mean-field approach, known as the Gutzwiller ansatz, which approximates the many-body wave function as the product of individual contributions at each site. Additionally, a more advanced ansatz has been developed that considers pairs of coupled sites, allowing for the exploration of regions in the phase space that are not accessible with the traditional ansatz. The second technique is based on tensor networks, specifically representing the state as a Matrix Product State (MPS), combined with the Time-Evolving Block Decimation (TEBD) algorithm. This technique is used to analyze the ground state properties and magnetic behavior of the system under the influence of an external magnetic field. Both techniques were evaluated within the context of a Bilinear-Biquadratic Heisenberg Hamiltonian, incorporating perturbative corrections to account for the quadratic Zeeman effect. The results of this work demonstrate that tensor networks, particularly MPS, provide a robust numerical technique for capturing the quantum phenomena exhibited by spin-1 bosons. The calculations of ground state energy and magnetization profiles confirm the effectiveness of tensor networks in representing the essential physics of the system. Furthermore, the investigation of entanglement properties reveals that the system's entanglement entropy obeys an area law, characteristic of gapped one-dimensional systems. Chirality and spin correlation observables were also explored, revealing relevant information about the system's behavior under various interaction parameters. The results are consistent with previous theoretical and numerical studies, highlighting the potential of tensor networks to address challenges in many-body quantum physics. This work introduces a novel numerical perspective within the context of Solid State research at the University of Valle, paving the way for future studies utilizing advanced tensor network techniques.

Key words: Tensor networks, MPS, quantum simulators, Mott-insulator, Gutzwiller's ansatz.

Contents

1 INTRODUCTION

The Bose-Einstein condensate (BEC) represents a fundamental milestone in the 20th century quantum physics[1;2]. The theory developed by Bose and Einstein in 1925 predicted the formation of a quantum state of matter in which a significant number of particles occupy the lowest energy state. This phenomenon, initially challenging to confirm experimentally due to the extremely required low temperatures, led to the development of revolutionary laser cooling techniques. These techniques enabled the experimental realization of BEC in dilute alkaline gases in 1995[3], opening new doors for the exploration of quantum phenomena at the macroscopic scale and triggering advances in areas such as high-precision interferometry[4] and the creation of extremely sensitive devices[5], as well as fostering the development of atomic control techniques[6], such as optical lattices[7;8], that offer unprecedented control and tunability of quantum systems for future research and applications.

The combination of Bose-Einstein condensates and optical lattices offers a unique platform to study strongly correlated regimes and complex quantum phenomena, providing valuable insights at the frontier of condensed matter physics[8]. Optical lattices, conceived as periodic Stark shift potentials generated by laser beam interference, have been fundamental in atomic physics, enabling diffraction, trapping and cooling of atoms[9]. In particular, these networks have been used to explore the fascinating world of quantum simulators within condensed matter[10]. Pioneering experiments, such as those performed by Hemmerich and Grynberg[11;12], have demonstrated the ability to cool atoms down to the micro-Kelvin regime in multidimensional optical lattices. Techniques such as laser cooling have succeeded in reducing atoms to their ground state with remarkable filling factors. However, a particularly successful strategy has been the loading of ultracold atoms into ground states by prior formation of a Bose-Einstein condensate in a weak magnetic trap, followed by adiabatic turn-on of the optical lattice[3;13]. This dynamics, inspired by band structure and Bragg scattering in crystalline solids, allows the controlled exploration of phenomena such as coherent matter-wave interferometry and the superfluid-insulator Mott phase transition[14].

The inclusion of the spin degree of freedom introduces an additional dimension of complexity and richness to the exploration of condensed matter[15]. By considering such particles, the door is opened to a wide range of fascinating and potentially useful physical phenomena. Spin-1 bosons exhibit unique properties, such as the presence of quadrupole magnetic modes[16]. Unlike magnetic dipoles that are characterized by a vector pointing in a specific direction, quadrupoles describe a more complex spatial arrangement of the spin states, leading to what is known as nematic order[17]. In this order, spins tend to align in a plane, exhibiting anisotropic fluctuations without generating net magnetization. This lack of net magnetization distinguishes quadrupolar order from typical magnetic ordering such as ferromagnetism or antiferromagnetism, where spins align or anti-align along a specific axis. Spin-1 systems allow for exploration of different phase transitions, such as from polar phases, which exhibit non-zero magnetization, to quadrupolar or nematic phases[18] that remain robust against external magnetic fields due to their lack of magnetization. The interplay between quadrupolar and dipolar interactions creates complex structures and phase transitions, offering rich collective magnetic phenomena and intricate magnetic structures, which have potential applications in quantum technologies[19].

The study of quantum spin chains presents significant challenges due to the difficulty of simulating systems with more than a few dozen particles. Even the most advanced supercomputers would be unable to compute an exact solution due to the exponential scalability of the problem. For a system of size N, the memory required to encode its state scales as 3^N, where 3 corresponds to the number of internal states. In the face of this complexity, numerous approximate numerical techniques have been developed in recent decades by physicists and mathematicians to better understand the relevant properties of quantum spin chains[20]. Among them is the Gutzwiller variational ansatz[21], which features as a mean-field approximation to describe complex quantum states and is further detailed throughout this document.

Tensor networks have emerged as a powerful technique for analyzing many-body systems in quantum mechanics, offering efficient solutions to the computational challenges inherent in such complex systems[22]. At their core, tensor networks represent the quantum state of a system using multidimensional tensors, effectively capturing correlations between particles. This approach provides a structured and compact representation of highly intricate states[23]. Moreover, tensor networks offer efficient methods for manipulating tensors, including contraction and decomposition, which streamline calculations of crucial physical properties such as energies, wave functions, and observables[24].

In this work, we leverage the versatility of tensor networks by utilizing Matrix Product States (MPS) to represent quantum states. MPS stands out as a particularly advantageous choice due to its

capability to efficiently approximate one-dimensional gapped systems, aligning perfectly with our focus on such systems. Furthermore, in tandem with the groundbreaking Density Matrix Renormalization Group (DMRG) algorithm, a class of algorithms has emerged for efficiently time-evolving MPSs under a nearest-neighbor Hamiltonian[25]. Notably, Time-Evolving Block Decimation (TEBD) is among the most prominent methods in this category, offering efficient handling of such evolutions. In our study, we harness the power of TEBD alongside MPS for a comprehensive analysis of quantum systems.

This thesis is structured to provide an exploration of quantum many-body theory applied to spinorial systems with an internal degree of freedom of spin-1. In Chapter 2, fundamental concepts are elucidated to construct a theoretical framework for our investigation. This sets the stage for our exploration of two distinct numerical methods in subsequent chapters. Chapter 3 delves into the analysis of the Heisenberg Bilinear Biquadratic Hamiltonian, reviewing initially the typical single-site Gutzwiller ansatz to solve coupled differential equations and determine ground state phases. This approach allows for the measurement of select observables crucial for understanding the system's behavior. Later, the possibility of expanding this ansatz to couple two lattices sites is explored. In Chapter 4, we shift our focus to tensor networks, showcasing their effectiveness in characterizing the same physical system. Leveraging the algebraic properties of tensor networks, we efficiently measure relevant observables and gain insight into the system's phases. Finally, we retrieve some conclusions about the numerical methods and the results by comparing the two Gutzwiller approaches versus the tensor network one.

2 Spin-1 physics

In this chapter, the goal is to introduce the physical system in which the numerical methods described in Chapters 3 and 4 will be tested. This system consists of a set of strongly correlated spin-1 particles trapped in an optical lattice in the Mott insulator regime. One of the important defining features of our system is the nature of the particles, which in this case have a spin of 1. To explore the implications of this for our system, we begin by introducing the Bose-Hubbard model for spinless particles trapped in a one-dimensional periodic potential. Then, we incorporate the spin degree of freedom and introduce a quadratic Zeeman field that partially lifts the degeneracy and reveals new magnetic phases. Finally, we restrict our system to the Mott insulator regime with unitary filling, recovering the effective Hamiltonian via van Vleck's second-order quasi-degenerate perturbation theory, which results in the bilinear-biquadratic Heisenberg model with an external quadratic magnetic field.

2.1 | Bose-Hubbard Hamiltonian

The Bose-Hubbard Hamiltonian stands out as the most basic yet non-trivial model for elucidating the behavior of interacting spinless bosons within a periodic potential. It encapsulates the essential physics governing strongly interacting bosons, highlighting the interplay between kinetic and interaction energies. Widely applied in solid-state physics, this model has successfully described various systems such as short correlation length superconductors, Josephson arrays, and the behavior of cold atoms confined in optical lattices[26;27].

The most naive approach we can propose when describing a system of N particles loaded in a one dimensional lattice is given by the general Hamiltonian of interacting particles, $\sum_{i=1}^{N}\left(\hat{T}_i+\hat{V}\right)+\frac{1}{2}\sum_{i,j=1}\hat{F}_{ij}$. Where $\hat{T}_i$ is the kinetic energy operator, $\hat{V}$ is a periodic potential and $\hat{F}_{ij}$ corresponds to the interaction potential. Nevertheless, this does not turn out to be the most appropriate formalism

to describe the physics of many-particle systems.

By resorting to the second quantization formalism we find a more convenient way to rewrite our Hamiltonian. Here, the basic entities are not wavefunctions of individual particles, as in first quantization, but rather field operators. These operators create or annihilate particles at specific quantum states and fulfills the bosonic commutation relations:

$$\hat{\Psi}(x) = \sum_i W_{R_i} \hat{b}_i, \qquad \hat{\Psi}^\dagger(x) = \sum_i W^*_{R_i} \hat{b}^\dagger_i. \tag{2.1}$$

$$\left[\hat{\Psi}(x), \hat{\Psi}^\dagger(x')\right] = \delta(x - x'), \qquad \left[\hat{\Psi}(x), \hat{\Psi}(x)\right] = \left[\hat{\Psi}^\dagger(x'), \hat{\Psi}^\dagger(x')\right] = 0. \tag{2.2}$$

Where we have chosen the position representation so that we can expand the field operators in terms of the Wannier functions $W_R(x)$: a set of functions highly localized on the $i-th$ lattice site, making them useful for expressing field operators in the second quantization formalism[28].

$$W_R(x) = \frac{1}{\sqrt{L}} \sum_k e^{-ik\cdot R} \psi_{kn}(x), \qquad \int W^*_R(x) W_{R'}(x) dx = \delta_{RR'}. \tag{2.3}$$

Here, $\psi_k(x)$ represents the Bloch states, L the number of sites, R the lattice constant and k the quasi-momentum with its values located on the first Brillouin zone.

The Hamiltonian written on the second quantization formalism takes the following form:

$$\hat{H} = \int dx \hat{\Psi}^\dagger(x) \left(\frac{-\hbar^2}{2m} \nabla^2 + \hat{V}(x) \right) \hat{\Psi}(x) + \frac{1}{2} \int dx dx' \hat{\Psi}^\dagger(x) \hat{\Psi}^\dagger(x') \hat{V}(x, x') \hat{\Psi}(x') \hat{\Psi}(x), \tag{2.4}$$

where it can be pointed out that the first part refers to the kinetic energy of the particles along with the induced periodic potential representing the lattice, while the second term captures the interaction between the particles through an effective pseudo-potential $\hat{V} = g\delta(x, x')$, where $g = \frac{4\pi\hbar^2 a}{2}$ manifest the strength of the interaction with a scattering length a.

Rewriting the Hamiltonian in a more convenient form,

$$\hat{H} = -J \sum_{\langle i,j \rangle} (\hat{b}^\dagger_i \hat{b}_j + h.c) + \frac{U}{2} \sum_i \hat{n}_i (\hat{n}_i + 1) - \mu \sum_i \hat{n}_i, \tag{2.5}$$

the first term accounts for the kinetic energy of bosons where $\hat{b}^\dagger_i, \hat{b}_j$ are bosonic creation and annihilation operators that allow the particles to tunnel between neighboring lattice sites. It is characterized by the hopping parameter J, representing the amplitude for particles to move from one site to another. The second term displays the interaction term, which reflects the repulsive forces

between bosons occupying the same lattice site. It is defined by the on-site interaction energy U, signifying the cost associated with having multiple bosons on a single site. Followed by the chemical potential term, denoted by μ, which introduces a potential energy contribution for adding or removing a boson from a given lattice. It controls the overall particle density and accounts for the conservation of the total number of particles.

Consistent with 2.4, the hopping and interaction parameters take the form:

$$J = \int W_i^*(x)\left(\frac{-\hbar^2}{2m}\nabla^2 + \hat{V}(x)\right)W_j(x), \qquad U = g\int dx|W(x)|^4. \tag{2.6}$$

It should be noted that the term associated with the chemical potential is introduced manually in 2.5 because it allows to fix the particle density, which is crucial when one wants to study the transition between different phases (such as the transition from superfluid to Mott insulator).

2.1.1 | Superfluid - Mott insulator Transition

At temperatures close to absolute zero (typically in the nanoKelvin order), the Bose-Hubbard Hamiltonian delineates two distinct scenarios. In the interaction-dominated regime, characterized by J significantly smaller than U, the system enters the Mott insulator phase. Conversely, in the kinetic energy-dominated regime, where tunneling prevails over repulsion, the system demonstrates superfluid characteristics. The emergence of superfluidity results from the interplay between kinetic energy, seeking particle delocalization, and interaction energy, aiming to localize particles and minimize number fluctuations.

In the superfluid regime, the Hamiltonian is mainly governed by the kinetic energy term, leading to negligible quantum correlations. This allows for an effective description of the system through a macroscopic wave function, where the many-body state approaches identical single-particle wave functions, reflecting a well-defined macroscopic phase indicative of superfluidity[29;30]. Atom delocalization over the lattice results in an interference pattern resembling a coherent array of matter wave sources when the lattice is turned off, such that the single particle wavefunction for N atoms can be written as,

$$|\Psi_{SF}\rangle \propto \left(\sum_{i=1}^{M}\hat{a}_i^\dagger\right)^N|0\rangle. \tag{2.7}$$

On the other hand, with increased interactions, the average kinetic energy for particle hopping decreases, rendering it insufficient to overcome potential energy costs. This results in atom localization at individual lattice sites, reducing number fluctuations. In the Mott insulator phase, the

system's ground state is characterized by localized atomic wave functions with fixed particle numbers per site,

$$|\Psi_{MI}\rangle \propto \prod_{i=0}^{M} \left(\hat{a}_i^{\dagger}\right)^n |0\rangle. \tag{2.8}$$

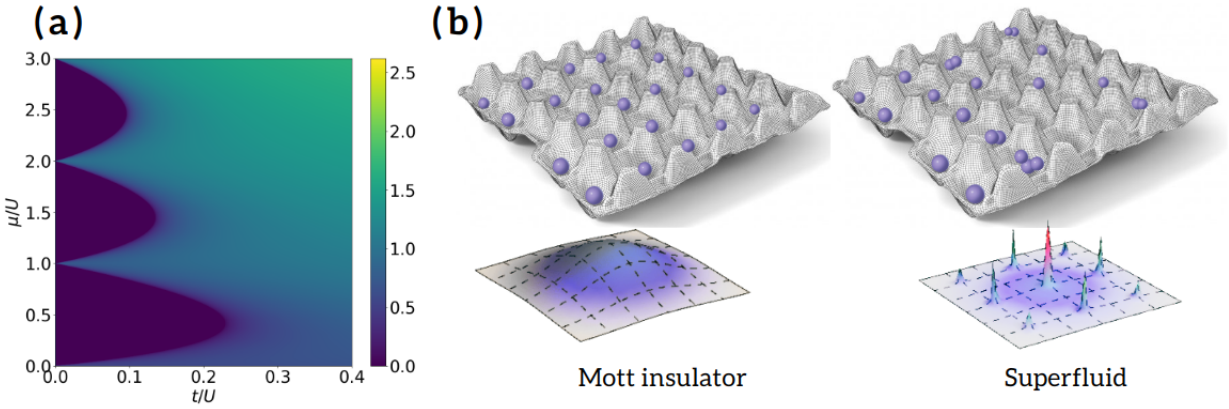

Figure 2.1: (a)Phase diagram for the Bose Hubbard model where $\langle \hat{n} \rangle$ is plotted as a function of t/U and μ/U exhibiting the Mott's insulator and superfluid phases showed in (b).

Figure 2.1 shows the Mott insulator transition of a translational invariant system in the $\frac{J}{U} - \frac{\mu}{U}$ plane[31]. The physics behind the diagram goes as follows: beginning within the Mott insulating phase and subsequently increasing $\frac{\mu}{U}$ while keeping $\frac{J}{U}$ constant, there exists a point where the kinetic energy associated with adding an extra particle and allowing it to move within the lattice equals the interaction energy cost. At this juncture, the introduction of an additional particle restores phase coherence, causing the system to transition into the superfluid regime. Conversely, when decreasing μ from a position within the Mott phase, there will be a point where it becomes energetically advantageous to remove a particle from the system.

2.2 | Spin-1 Hamiltonian

Following the same logic of the Bose Hubbard Hamiltonian described above, we write a Hamiltonian characterizing the interaction of spin-1 bosons, such that in principle we also have three terms alluding to the hopping, the interaction, and the chemical potential,

$$\hat{H} = \hat{H}_0 + \hat{H}_I + \hat{H}_\mu, \tag{2.9}$$

the hopping term $\hat{H}_0$ that accounts for the probability of particles tunneling from one site to another between neighboring sites is written in terms of the bosonic creation and annihilation operators,

$$\hat{H}_0 = -J \sum_{i,j,\sigma} \left(\hat{b}^\dagger_{j,\sigma} \hat{b}_{i,\sigma} + \hat{b}^\dagger_{i,\sigma} \hat{b}_{j,\sigma} \right), \tag{2.10}$$

where the operators $\hat{b}^\dagger_{i,\sigma}(\hat{b}_{i,\sigma})$ create (annihilate) bosons with internal degree of freedom $\sigma = -1, 0, 1$ in the i-site.

The next step consists of building the interaction Hamiltonian and for this, we consider the simplest possible case which corresponds to computing the interaction of two spin-1 bosons. In this case, the natural basis to describe this scenario is the coupled one, given by the addition of angular momentum,

$$|S_1, S_2, S, m_s\rangle \quad \rightarrow \quad \hat{S}_1, \hat{S}_2, \hat{S}^2, \hat{S}_z,$$

since $S_1 = S_2 = 1$, the possible values for S are $0, 1, 2$. However, due to the symmetric nature of bosons the only allowed values are $S = 0, S = 2$, such that from the whole set of states spanning the Hilbert space for the two-particle interaction we only preserve,

$$\begin{aligned}
|2,2\rangle &= |1,1\rangle \\
|2,1\rangle &= \sqrt{\frac{1}{2}}|0,1\rangle + \sqrt{\frac{1}{2}}|1,0\rangle \\
|2,0\rangle &= \sqrt{\frac{1}{6}}|-1,1\rangle + \sqrt{\frac{2}{3}}|0,0\rangle + \sqrt{\frac{1}{6}}|1,-1\rangle \\
|2,-1\rangle &= \sqrt{\frac{1}{2}}|0,-1\rangle + \sqrt{\frac{1}{2}}|-1,0\rangle \\
|2,-2\rangle &= |-1,-1\rangle \\
|0,0\rangle &= \sqrt{\frac{1}{3}}|-1,1\rangle + \sqrt{\frac{1}{3}}|0,0\rangle + \sqrt{\frac{1}{3}}|1,-1\rangle.
\end{aligned} \tag{2.11}$$

We restrict ourselves to a contact pseudo-potential interaction type motivated by the low energy regime, in which particles scatter off each other when occupying the same position, where we only take into account the first term in the partial wave expansion, hence s-wave scattering[32]. Now, the on-site interaction is expressed in terms of two interacting channels $F = 0, 2$ using the projector operators $\hat{P}_F = \sum \langle S, m_s | S, m_s \rangle$, we can express the potential energy as:

$$\hat{V} = \sum_F \hat{V}^2 = \frac{4a_F\pi\hbar^2}{2} \sum_F \hat{P}_F \delta(r - r') \tag{2.12}$$

From the second quantization treatment of our general Hamiltonian[33], we found that the interacting part looked like,

$$\hat{H}_I = \frac{1}{2} \sum_{ijkl} \hat{b}^\dagger_{i,\sigma} \hat{b}^\dagger_{j,\sigma} \langle ij| \hat{V}_I |kl\rangle \hat{b}_{l,\sigma} \hat{b}_{k,\sigma}, \tag{2.13}$$

where $\hat{V}_I = \sum_F g_F \hat{P}_F \delta(r_2 - r_1)$, being $g_F = \frac{4a_F\pi\hbar^2}{m}$. Introducing all the projectors of the symmetric states defined in 2.11 we obtain the full interaction term which describes two categories of interactions between spin-1 particles during collisions: spin-preserving and spin-changing collisions. Spin-preserving collisions involve two particles interacting, leading to two outgoing particles with identical spin projections. In spin-changing collisions, particles alter their spin projections during the collision while preserving the total spin projection. However, the conservation of the total spin projection is maintained throughout the entire process in both scenarios,

$$\begin{aligned} \hat{H}_I = \sum_i \Bigg[& \frac{g_2}{2} \Big(\hat{b}^\dagger_1 \hat{b}^\dagger_1 \hat{b}_1 \hat{b}_1 + \hat{b}^\dagger_{-1} \hat{b}^\dagger_{-1} \hat{b}_{-1} \hat{b}_{-1} + 2\hat{b}^\dagger_1 \hat{b}^\dagger_0 \hat{b}_1 \hat{b}_0 + 2\hat{b}^\dagger_{-1} \hat{b}^\dagger_0 \hat{b}_{-1} \hat{b}_0 \Big) \\ & + \frac{g_0 + 2g_2}{6} \hat{b}^\dagger_0 \hat{b}^\dagger_0 \hat{b}_0 \hat{b}_0 + \frac{g_2 - g_0}{3} \Big(\hat{b}^\dagger_1 \hat{b}^\dagger_{-1} \hat{b}_0 \hat{b}_0 + \hat{b}^\dagger_0 \hat{b}^\dagger_0 \hat{b}_1 \hat{b}_{-1} \Big) \\ & + \frac{2g_0 - g_2}{3} \hat{b}^\dagger_1 \hat{b}^\dagger_{-1} \hat{b}_{-1} \hat{b}_1 \Bigg]_i . \end{aligned} \tag{2.14}$$

Putting all terms together, we obtain the final Hamiltonian,

$$\hat{H} = -J \sum_{i,j,\sigma} \Big(\hat{b}^\dagger_{j,\sigma} \hat{b}_{i,\sigma} + \hat{b}^\dagger_{i,\sigma} \hat{b}_{j,\sigma} \Big) + \hat{H}_I - \mu \sum_{i,\sigma} \hat{n}_{i\sigma} + Q \sum_{i,\sigma} \sigma^2 \hat{n}_{i,\sigma}. \tag{2.15}$$

Here we have added a term describing a quadratic Zeeman effect (QZE), where Q represents the strength of the quadratic Zeeman field with the constrain $Q \sim t^2/U$, motivated by the fact that in the condensed matter realm, two forms of field symmetry breaking are explored: the linear Zeeman effect and the quadratic Zeeman effect. Although the linear effect is remarkable, the quadratic field allows us to unveil the fascinating features of the spin-changing collisions non-present in spin-1/2 systems and emerging naturally in these spin-1 systems, where quantum fluctuations have a more pronounced influence. Unlike the linear Zeeman effect, the quadratic Zeeman effect in 1D systems gives rise to more intriguing phenomena, making it an area of special interest in quantum systems research[34;35;36]. Furthermore, in experimental settings, magnetic fields tend to oscillate rapidly in time[37], resulting in effects that cancel out on average. In contrast, the quadratic Zeeman effect

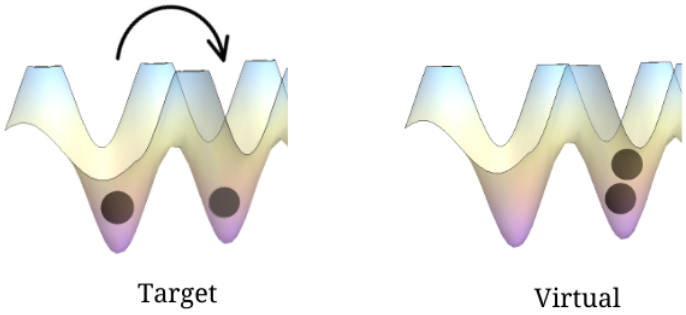

Figure 2.2: Representation of a 1D optical lattice loaded with two particles, before (target) and after (virtual) hopping.

provides more complex and captivating results. This phenomenon reveals itself in a particularly intriguing way in one-dimensional (1D) systems.

2.3 | Bilinear Biquadratic Heisenberg Hamiltonian

As mentioned in the previous section, the Bose-Hubbard model is characterized by two phases, and in this work, we are interested in studying the regime of strong interactions in the Mott insulator phase, so the kinetic term must be treated perturbatively to obtain the effective Hamiltonian that captures the desired physics, which in fact is the generalized Heisenberg model for spin 1 particles[], and thus allows a focus on the magnetic properties of the system.

Our starting point is the Hamiltonian for a system of spin-1 bosons described by equation 2.15. We begin by defining the basis for a reduced system that reproduces the dynamics of interest, which corresponds to a two-celled lattice with two particles,

The unperturbed Hamiltonian is then diagonalized and second order quasi-degenerate perturbation theory (see Appendix A) is applied to obtain an effective Hamiltonian that captures the physics of the Mott insulator. The matrix elements of the effective Hamiltonian up to second order are given by:

$$\langle m|H^{(2)}|m'\rangle = \frac{1}{2}\sum_{l}\langle m|H_t|l\rangle\langle l|H_t|m'\rangle\left[\frac{1}{E_m - E_l} + \frac{1}{E'_m - E_l}\right], \tag{2.16}$$

where $|m\rangle$ are two-site states with one particle per site (target states) and $|l\rangle$ are the two-site states with two particles on a single site and an empty site (virtual states) as showed in the Figure 2.2(a) and (b) respectively.

Since we are considering a small hopping amplitude J, the interaction is restricted to the nearest neighbors. Then, we can express the obtained matrix for the effective Hamiltonian in terms of S=1 spin operators, which happens to coincide with the Bilinear Biquadratic Heisenberg Hamiltonian, which is known as a generalized Heisenberg model and is commonly parameterized as:

$$\hat{H} = -J \sum_i \left[\cos(\theta) \hat{S}_i \cdot \hat{S}_{i+1} + \sin(\theta) \left(\hat{S}_i \cdot \hat{S}_{i+1} \right)^2 \right] - \sum_i JD(\hat{S}_i^z)^2, \tag{2.17}$$

where, $\cos\theta$ gives the strength of the bilinear coupling and $\sin\theta$ of the biquadratic one. Here we have added the quadratic Zeeman term, for which $D = -Q/J$ with the main purpose of magnify the magnetic properties of the system as described in 2.3.1. As shown in ref.[16], the appearance of quadrupole degrees of freedom is equivalent to the fact that the interaction Hamiltonian contains the biquadratic term in spin operators, so that this Hamiltonian allows for the description of the quadrupolar degrees of freedom present in the system.

2.3.1 | Phases of the Bilinear Biquadratic Heisenberg model

Over the years, considerable attention has been devoted to the study of spin-1 bilinear biquadratic models. This goes back to the initial construction of an exact ground state[38] of the spin-1 BBH chain at $\theta = \arctan(1/3)$ in the middle of the Haldane phase[39], as well as the development of a form of spin wave theory by Papanicolaou[15], which is readily applicable to spin-1 BBH models in bipartite lattices.

In the one-dimensional context, the spin-1 bilinear-biquadratic model without the external magnetic field (D=0), exhibits a complex and diverse phase diagram (see Figure 2.3(a)). This diagram includes some well-established phases, such as the Haldane gaped phase[40], a dimerized phase[39], and a ferromagnetic phase. In addition, lesser-known phases have been identified, such as the critical phase with dominant nematic spin correlations[41]. In this case, the properties of the ground state are entirely determined by an angle θ[42].

Here, we want to explore some properties of the induced phases by the quadratic Zeeman field ($D \neq 0$) in the Mott insulator regime shown in Figure 2.3(b). On the one hand, there is the ferromagnetic regime composed of 3 phases: Ising, Large-D and XY-Ferromagnetic. It can be seen that the Ising-FM can be reached for ($\theta < \frac{-3\pi}{4}$) and $D > 0$. In this phase, the fundamental state is dominated by magnetic projections of spin $m = 1, -1$ aligned along the external field axis. Meanwhile, for $D < 0$ the Large-D phase is characterized by a vanished total magnetization, where the spin projection $m = 0$ dominates, implying a lack of significant magnetic response in principal terms. Nevertheless, there is another phase, for small values of $|D|$ with $D < 0$, called $XY-FM$ phase, where the fundamental state is characterized by a combination of all magnetic spin projections, where the

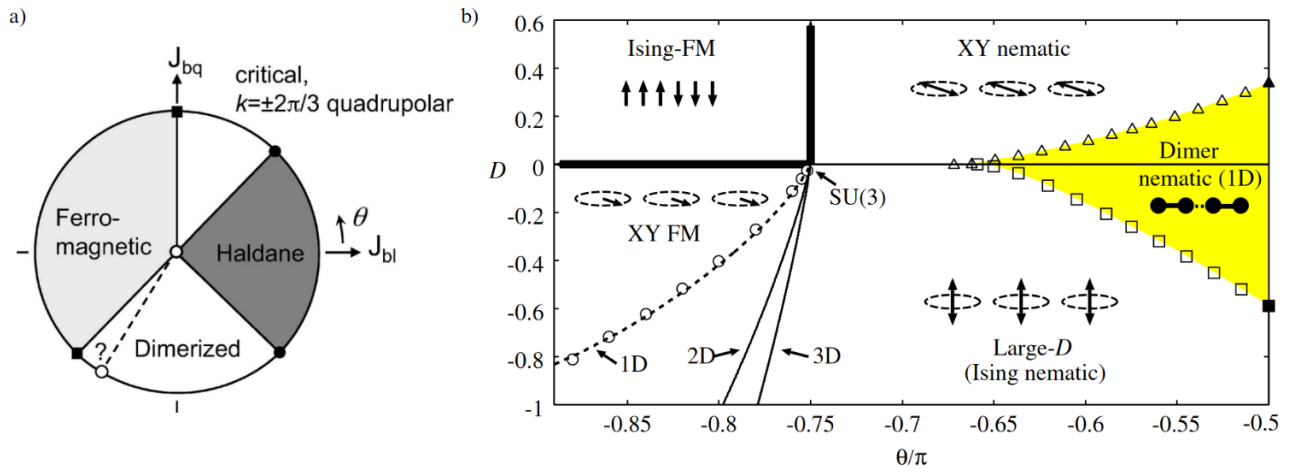

Figure 2.3: Phase space diagram for the spin-1 bilinear-biquadratic Heisenberg model at unit filling a) in the absence of an external quadratic Zeeman field and as a function of θ. The well-established phases are the Haldane phase, the ferromagnetic phase and the dimerized phase.[43]. b) in the presence of an external quadratic Zeeman field[44].

probability of having 0 spin projections is slightly greater than the probability of having ± 1 projections. The system also presents an antiferromagnetic region (AFM) for $\theta > 3\pi/4$, in which we can see that for a $D > 0$ field an XY-nematic phase is induced. Here projections $m = \pm 1$ are equally biased, which results in the system being in a superposition of these states. Therefore, there is no preferred direction for the system, rather it is defined by an axis or director.

A critical aspect of exploring the physical system outlined above lies in the ability to discern how properties of its phases behave. Therefore, the next two chapters are dedicated to the development of numerical methods aimed at reaching the ground state of the system, among other objectives, and subsequently applying various observables. Chapter 3 focuses on employing the Gutzwiller ansatz, which enables the solution of coupled differential equations and facilitates the identification of ground state phases. This method is instrumental in understanding the behavior of the system and allows for the measurement of key observables crucial for characterizing its phases. In Chapter 4, an alternative and yet more powerful numerical approach using tensor networks, specifically Matrix Product States (MPS), is introduced. This method offers a structured representation of quantum states, allowing for efficient anzats for the system representation by means of symmetry implementations and tensorial properties for the linear algebra calculations, just to mention only a few. This technique also allow us to optimize measurements of observables and providing additional insights into the phases of the system.

3 Gutzwiller Variational Ansatz

The Gutzwiller ansatz is a well-established method in the field of many-body quantum mechanics. It is particularly useful for studying strongly correlated systems, where the traditional mean-field theory fails to capture the full complexity of the interactions between particles[45]. By incorporating variational parameters and a Gutzwiller projection, the ansatz allows for a more accurate description of the ground state properties of these systems. The Gutzwiller ansatz has proven to be effective in investigating a wide range of phenomena, such as metal-insulator transitions, magnetism, and high-temperature superconductivity. Its ability to capture the effects of correlations and adapt to different interaction strengths makes it a valuable tool in understanding the behavior of complex materials and quantum many-body systems[46].

3.1 | One-site Gutzwiller ansatz

The Gutzwiller mean-field method has found extensive application in various research papers focused on the Bose-Hubbard model. In its most basic form, this method relies on approximating the many-body wave function by multiplying individual site contributions as:

$$|\Psi\rangle = \prod_i \sum_{n=0}^{n_{max}} f_{n_i}^i |n_i\rangle \tag{3.1}$$

where $|n_i\rangle$ denotes the Fock state of n atoms in the i-th lattice site, n_{max} is a system size-independent cut off in the number of atoms per site, and f_n^i corresponds to the amplitude of having n atoms in the i-th lattice site, which in this case corresponds to complex time-dependent coefficients. The amplitudes are normalized to $\sum_n |f_{n_i}^i|^2 = 1$. In the dynamical case, these amplitudes can be found by considering the variational principle, minimizing of the action of the system giving by $S = \int dt\mathcal{L}$. The Lagrangian associated to the Hamiltonian is given in[47] and looks like:

$$\mathcal{L} = \frac{i\hbar}{2}\Big(\langle\Psi|\dot{\Psi}\rangle - \langle\dot{\Psi}|\Psi\rangle\Big) - \langle\Psi|\hat{H}|\Psi\rangle. \tag{3.2}$$

The dynamical equations can be retrieved from the Euler-Lagrange formulation [48],

$$\frac{d}{dt}\left(\frac{d\mathcal{L}}{d\dot{f}^{*i}_{n_i}}\right) = \frac{d\mathcal{L}}{df^{*i}_{n_i}}. \tag{3.3}$$

After implementing the aforementioned steps and performing the corresponding algebraic procedures for the spinless Bose-Hubbard model with nearest neighbor interaction [see Appendix A], the dynamics can be characterized by the following set of coupled differential equations,

$$\begin{aligned} i\hbar\frac{d}{dt}f_n^{(i)} = &-t\sum_m\Big[\sqrt{n}\sqrt{m}f_{n-1}^{(i)}\left(f_{m-1}^{*(i+1)}f_m^{(i+1)} + f_{m-1}^{*(i-1)}f_m^{(i-1)}\right) \\ &+\sqrt{n+1}\sqrt{m}f_{n+1}^{(i)}\left(f_m^{*(i+1)}f_m^{(i+1)} + f_m^{*(i-1)}f_{m-1}^{(i-1)}\right)\Big] \\ &+\frac{U}{2}f_n^{(i)}n(n-1) - \mu f_n^{(i)}n, \end{aligned} \tag{3.4}$$

where the i index runs over the L lattice sites, n and m correspond to the internal degree of freedom (number of particles in this case), where $n, m = 0, 1, 2$ since the maximum allowed number of particles per site is two, for keeping ourselves up to the first Mott-insulator lobe ranging the full t/U axis.

In this work, particles with spin-1 are considered, such that the index associated to the internal degrees of freedom is now associated to the possible magnetic projections of the particles at each site, when we focus on the Mott-insulator regime with one particle per site

$$|\Psi\rangle = \prod_i \sum_{m=-1}^{m=1} f^i_{m_i}|m_i\rangle. \tag{3.5}$$

Since the study of the phases is based on the biquadratic bilinear Heisenberg Hamiltonian, an approximation of the Bose-Hubbard model for spin-1 particles confined in the Mott insulator allowing only one particle per site; each site exhibit exclusively the three degrees of freedom related to the magnetic projections of the particle located at that site.

3.2 | Imaginary Time Evolution

In the realm of quantum many-body problems, the imaginary-time evolution method stands as a well-established computational approach, adept at singling out the ground-state component through temporal evolution along the imaginary time axis. Imaginary time, though an unphysical yet potent mathematical concept, finds widespread utility across various physical domains, encompassing

quantum mechanics[49], statistical mechanics[50], and cosmology[51]. Often referred to as a Wick rotation, the substitution of real-time with imaginary time establishes connections between Euclidean and Minkowski space, quantum and statistical mechanics, and static problems with dynamic counterparts[52]. In the realm of quantum mechanics, the propagation of a wavefunction in imaginary time facilitates the exploration of finite-temperature properties, the determination of ground-state wavefunctions and energies, and the simulation of real-time dynamics[53].

As we know, time evolution in quantum mechanics is governed by the Schrödinger equation,

$$i\hbar\frac{\partial\psi(x,t)}{\partial t} = \hat{H}\psi(x,t). \tag{3.6}$$

When the Hamiltonian is time-independent, then it is feasible to solve the above equation to find the time dependence of $\Psi(x,t)$. What you need to do is first solve the eigenvalue equation for the Hamiltonian $\hat{H}\psi_n(x) = E_n\psi_n(x)$, where $\psi_n(x)$ are the eigenstates and E_n the energy eigenvalues. Second, we need to expand the wave function at an initial time (say $t = 0$) in terms of the energy eigenstates:

$$\psi(x,0) = \sum_n c_n(0)\psi_n(x), \tag{3.7}$$

where $c_n(0)$ are the expansion coefficients that can be found by calculating the overlap between $\psi(x,0)$ and the energy basis eigenstates. Third, the wave function at a later time t is given by:

$$\psi(x,t) = \sum_n c_n(0)e^{-\frac{i}{\hbar}E_n t}\psi_n(x). \tag{3.8}$$

The time dependence is such that each energy eigenstate $\psi_n(x)$ "oscillates" at a frequency proportional to the corresponding energy eigenvalue $E_n/\hbar$. Now, considering a change of variables $\tau = it$. One can think of τ as "imaginary time". Applying this change of variables to the Schrödinger equation we obtain:

$$-h\frac{\partial\psi(x,\tau)}{\partial\tau} = \hat{H}\psi(x,\tau). \tag{3.9}$$

Again, as $\hat{H}$ is time-independent, the dependence on τ can be solved in the same way in which the dependence on t was solved above, and we obtain:

$$\psi(x,\tau) = \sum_n c_n(0)e^{-\frac{i}{\hbar}E_n\tau}\psi_n(x), \tag{3.10}$$

it can be seen that the function $\psi(x,\tau)$ at imaginary time τ is no longer obtained by an oscillating superposition of energy eigenstates, but instead by an exponentially decaying superposition of

energy eigenstates. Furthermore, the exponential decay rate is proportional to E_n.

What have we accomplished by making this variable change from t to τ? Consider the limit of large τ:

$$\psi(x, \tau \gg 1) \simeq c_0(0) e^{-E_0 \tau} \psi_0(x). \tag{3.11}$$

In this limit, the ground state $n = 0$ is projected out to the initial state, because the corresponding exponential decay is the slowest one. Therefore, by evolving the system in imaginary time, we can obtain the ground state of the Hamiltonian $\psi_0(x)$ as the long imaginary time limit. To obtain the ground state of the system from the set of differential equations obtained in 3.4, the Runge-Kutta 4th order method, an iterative method used to solve ordinary differential equations, was implemented.

Performing the change in the time coordinate by the definition of imaginary time defined above, the expression defining the system is given by,

$$i\frac{df}{d\tau} = G(f, -i\tau). \tag{3.12}$$

The code loops over the set of equations until the energy minimization criterion is reached, following the flowchart3.1·

3.2.1 | Code implementation

The implementation of the method was done following the steps of the code written in C++ proposed by Rodriguez in[54] and structurally consists of 4 steps to find the energy (see Fig.3.1). First, the trial state is initialized with the values given by the balanced mixture, then the system is evolved using the RK-4 with the respective Wick rotation. Due to the non-unitarity of the previous step, the function is renormalized after each step and the convergence of the energy is evaluated by comparing the two consecutive values of the energy (from the previous and the current step) according to the established convergence criterion. This energy renormalization process is subject to the numerical technique being used. In the case of tensor networks, our next numerical technique, more specifically TEBD, no normalization is required thanks to the Suzuki-Trotter decomposition applied to the time evolution operator (see Chapter 4).

3.3 | Two-sites Gutzwiller Method

Here we aim to describe a natural extension of the Gutzwiller ansatz to a two-site ansatz where the variational state is expressed as the tensor product of the Gutzwiller wavefunctions of two neigh-

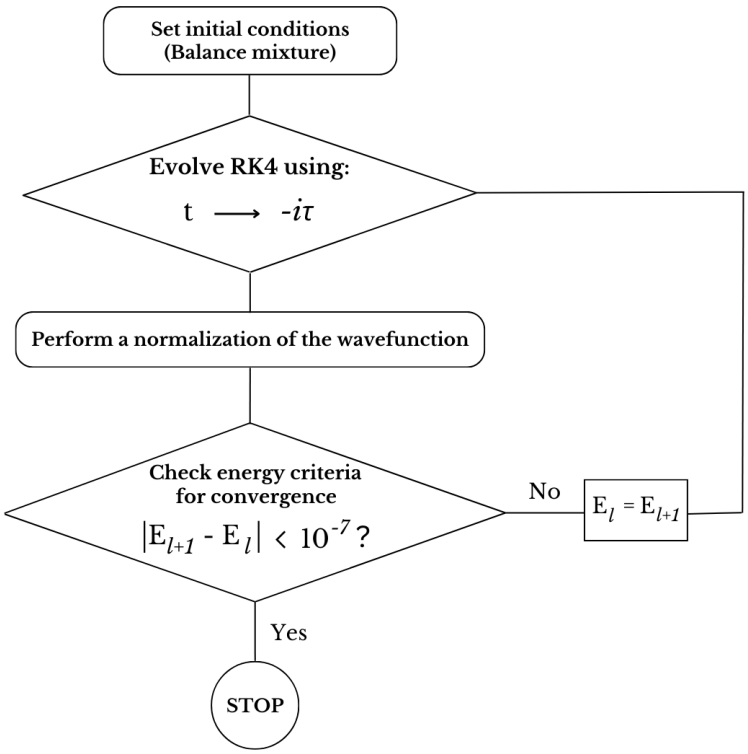

Figure 3.1: Flowchart of the Gutzwiller variational method numerical implementation.

boring sites, and there is only one coefficient associated with this two-site state implying the non-separabity among them as shown in Eq.3.16. This type of ansatz simplifies the state by considering inherent shared information between two adjacent sites in the lattice, and it's a natural approach in variational methods for studying strongly correlated systems, since it respects all Hamiltonian symmetries.

The two-site unit cell to be considered is now the one shown in the top of Figure 3.2, such that site i is now composed of two sub-sites and the full ansatz can be written as:

$$|\psi\rangle = \prod_i \sum_{m_a,m_b} f^i_{m_a,m_b} |m_a, m_b\rangle. \tag{3.13}$$

One of the motivations behind the extension is related to the physical model we are studying, in our case the biquadratic bilinear Heisenberg Hamiltonian (see Fig.2.15). This model exhibits entanglement between spins, and a two-sites ansatz has the potential to better capture such entanglement by considering correlations between neighboring spins. This could be important for accurately describing the properties of the ground state.

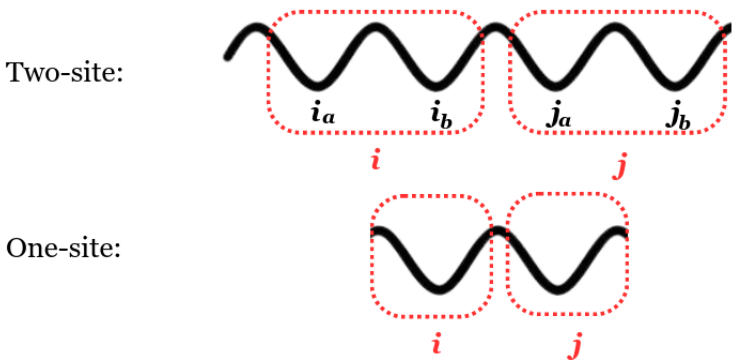

Figure 3.2: Pictorial representation of the new definition of 'site' for the extended Gutzwiller compared to the usual definition for a single site.

A similar development was performed as in the previous section to obtain the differential equations, but this time the operators take the form:

$$\hat{S}^i_\alpha \cdot \hat{S}^j_\gamma = \left(\hat{S}^{i_a}_\alpha + \hat{S}^{i_b}_\alpha\right) \cdot \left(\hat{S}^{i_a}_\gamma + \hat{S}^{i_b}_\gamma\right), \tag{3.14}$$

where, $\hat{S}^{i_{a,b}}_\alpha$ are the spin-1 operators acting at each sub-site. This led to the set of equations shown in Appendix B.

We can see, by comparison of the cosine term of the Hamiltonian for example, how the extension to two sites modifies the number of terms in the Hamiltonian but nevertheless retains some symmetry.

One site:

$$-J\sum_{\langle ij\rangle}\sum_m \cos\theta\Big[\sum_i \Big(f^i_n|f^{i+1}_m|^2 m\cdot n + f^i_n|f^{i-1}_m|^2 m\cdot n\Big)$$
$$+\Big(\frac{1}{2}f^i_{n-1}\sqrt{2-n(n-1)}\cdot f^{i+1}_m f^{*i+1}_{m-1}\sqrt{2-m(m-1)} + \frac{1}{2}f^i_n\sqrt{2-(n+1)n}\cdot f^{i-1}_m f^{*i-1}_{m+1}\sqrt{2-(m+1)m}\Big)$$
$$+\Big(\frac{1}{2}f^i_{n+1}\sqrt{2-(n+1)n}\cdot f^{i+1}_m f^{*i+1}_{m+1}\sqrt{2-(m+1)m} + \frac{1}{2}f^i_n\sqrt{2-(n+1)n}\cdot f^{i+1}_m f^{*i+1}_{m-1}\sqrt{2-m(m-1)}\Big]$$

Two sites:

$$-\mathrm{J}\sum_{ij} cos\theta\Big[\sum_{m_a m_b} f^{i}_{n_a n_b}|f^{i+1}_{m_a m_b}|^2(n_a+n_b)(m_a+m_b)+f^{i}_{n_a n_b}|f^{i-1}_{m_a m_b}|^2(n_a+n_b)(m_a+m_b)$$
$$+\frac{1}{2}\sum_{m_a m_b}\left(f^{i}_{n_a-1 n_b}\sqrt{2-(n_a-1)n_a}+f^{i}_{n_a n_b-1}\sqrt{2-(n_b-1)n_b}\right)\left(f^{i+1}_{m_a m_b}f^{*i+1}_{m_a-1 m_b}\sqrt{2-m_a(m_a-1)}\right.$$
$$\left.+f^{i+1}_{m_a m_b}f^{*i+1}_{m_a m_b-1}\sqrt{2-m_b(m_b-1)}\right)+\left(f^{i-1}_{m_a m_b}f^{*i-1}_{m_a+1 m_b}\sqrt{2-m_a(m_a+1)}+f^{i-1}_{m_a m_b}f^{*i-1}_{m_a m_b+1}\sqrt{2-m_b(m_b+1)}\right)$$
$$\left(f^{i}_{n_a n_b}\sqrt{2-(n_a+1)n_a}+f^{i}_{n_a n_b}\sqrt{2-(n_b+1)n_b}\right)+\frac{1}{2}\sum_{m_a m_b}\left(f^{i}_{n_a+1 n_b}\sqrt{2-(n_a+1)n_a}+f^{i}_{n_a n_b+1}\sqrt{2-(n_b+1)n_b}\right)$$
$$\left(f^{i+1}_{m_a m_b}f^{*i+1}_{m_a+1 m_b}\sqrt{2-m_a(m_a+1)}+f^{i+1}_{m_a m_b}f^{*i+1}_{m_a m_b+1}\sqrt{2-m_b(m_b+1)}\right)+\left(f^{i-1}_{m_a m_b}f^{*i-1}_{m_a-1 m_b}\sqrt{2-m_a(m_a-1)}\right.$$
$$\left.+f^{i-1}_{m_a m_b}f^{*i-1}_{m_a m_b-1}\sqrt{2-m_b(m_b-1)}\right)\left(f^{i}_{n_a n_b}\sqrt{2-(n_a-1)n_a}+f^{i}_{n_a n_b}\sqrt{2-(n_b-1)n_b}\right)\Big].$$

The first observation is that, as can be seen, the number of terms has doubled, but the important detail is that now the coefficients have two indices associated to the sub sites a and b for each site i of the lattice. Following the same logic, the extension for the entire Hamiltonian is developed. However, given the number of terms to evaluate and considering that this time we had to evaluate the magnetic projections for both m_a and m_b, a symbolic code was developed in Python to run the evaluations and return the simplified set of equations ready for the energy minimization process. The code presents a structure organized as scheme 3.3.

```
def Gutz_coef(f,j,m):
    define the coeffs and it's conjugate with the respective boundary conditions

def sin(f,N,n,M,m):
def cos(f,N,n,M,m):
def D(f,N,n,M,m):
        Define the three terms
          in the Hamiltonian


def sum(sin_output,cos_output,D_output,N,n,M,m):
    for N in range(-1,2):
       for n in range(-1,2):
          for M in range(-1,2):
             for m in range(-1,2):


⟶ return the terms of the energy already evaluated in the respective magnetic
    projections
```

Figure 3.3: Python implementation pseudocode to simplify summations over magnetic projections. Here the functions sin, cos and D corrresponds to the three terms of the Hamiltonian preceded by the respective constants, where N, n run over the values of the magnetic projections n_a, n_b and M, m run over m_a, m_b The range goes from -1 to 2 denoting the three magnetic projections and the correspondence is $0 \rightarrow |-1\rangle, 1 \rightarrow |0\rangle, 2 \rightarrow |1\rangle$.

In the study of the Bilinear Biquadratic Heisenberg model, excitations, collective spin modes, and entanglement are fundamental aspects that dictate the low-energy physics and quantum behavior of the system. The choice of ansatz in variational methods like the Gutzwiller ansatz significantly influences how these phenomena are represented in the wavefunction. By extending the ansatz to include correlations between neighboring sites, a two-site ansatz provides a more accurate description of collective spin modes and low-energy excitations compared to a one-site ansatz. This enhanced representation captures the coherent motion of spins across the lattice and accounts for quantum entanglement effects between adjacent spins. As a result, the two-site ansatz offers a comprehensive understanding of the low-energy physics of the model, shedding light on the behavior of strongly correlated spin systems and the intricate interplay between quantum phenomena such as entanglement and collective spin dynamics.

This extension of the traditional ansatz to a two-site ansatz can be compared with other types of methods that aim to study quantum many-body systems. In this work it has been compared with the MPS, because although they are fundamentally different approaches with different mathematical formulations, both techniques involve variational optimization to find the parameters that best minimize the energy. Furthermore, in principle both can capture correlations between neighboring sites and can capture some degree of entanglement with different complexity levels in both comprehension and implementation.

4 Tensor Networks

Tensor networks (TN), such as matrix product states (MPS), are invaluable tools in tackling the complexity of quantum many-body lattice systems[55]. These systems pose a challenge due to the exponential growth of the Hilbert space, making their theoretical and numerical exploration daunting. However, structured patterns in physically relevant states offer avenues to overcome this complexity, with tensor networks providing a crucial framework for their analysis[56].

In this chapter, we look into the Matrix Product State (MPS) representation, a key player in the realm of tensor networks[57;58]. Our exploration extends to comparing MPS with alternative ansatz methods like the Gutzwiller ansatz. By understanding the strengths and limitations of each approach, we gain insights into their applicability in describing quantum many-body systems.
Furthermore, alongside the static description provided by MPS and other tensor network representations, we explore the dynamic evolution of quantum systems. This exploration is facilitated by methods such as the Time-Evolving Block Decimation (TEBD) algorithm. TEBD enables efficient simulations of imaginary-time evolution, complementing the static analysis and providing a comprehensive understanding of quantum dynamics within tensor network frameworks.

Throughout our discussion, we anchor our exploration in the specific physical system described on Chapter 3: a one-dimensional array of spin-1 particles confined to an optical lattice, which we characterized by the Bilinear Biquadratic Heisenberg Hamiltonian, serving as a concrete example to illustrate the concepts and methodologies discussed in this chapter.

4.1 | Tensor network theory

In a more precise definition, a tensor is a mathematical object that generalizes concepts like scalars, vectors, and matrices. It is characterized by multiple indices (T_{ijklm}), and its components represent

quantities that transform in a specific way under coordinate transformations. In tensor network notation a single tensor is simply represented by a geometric shape with legs sticking out of it, each corresponding to an index, analogous to the indices of Einstein notation as shown in Figure 4.1 (a)[57].

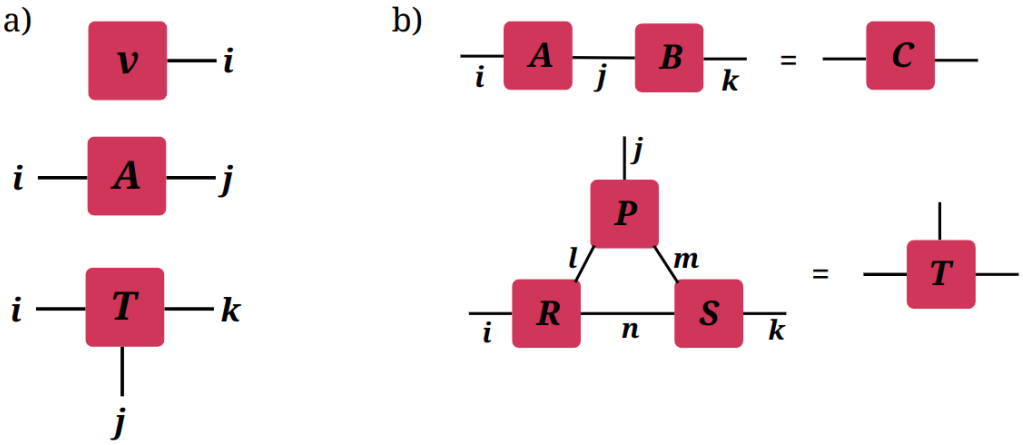

Figure 4.1: Tensor network diagrams. The 3 figures in (a) show the representation of a vector v, matrix A and rank-3 tensor T. The diagrams in (b) show a matrix-matrix product (boxes sharing legs) and a general contraction.

This new representation allows us to perform different operations, one of the most usual and general ones being contractions. For instance, the matrix product

$$C_{ik} = \sum_j A_{ij} B_{jk}, \tag{4.1}$$

corresponds to the contraction of the index j, and can be represented for the top diagram on Figure 4.1(b). Contractions are essential operations that facilitate the efficient manipulation and analysis of complex quantum states. These networks often involve the connection of multiple tensors, each associated with different physical degrees of freedom in a quantum system. The contraction process combines these tensors by summing over shared indices, effectively reducing the overall dimensionality of the system.

4.2 | Matrix Product State

In our exploration of tensor networks for our one-dimensional system, the Matrix Product State (MPS) stands out as the most suitable choice[59]. Its selection is motivated by distinct advantages that differentiate it from alternative methods, particularly the Gutzwiller ansatz we explored above.

One notable difference lies in the measurement of entanglement between subsystems. MPS offers a straightforward approach to computing entanglement entropy, thanks to its numerical structure closely mirroring the physical system. This characteristic facilitates the quantification of entanglement between different parts of the system, providing valuable insights into the underlying quantum correlations. Contrastingly, the Gutzwiller ansatz, while effective in capturing certain aspects of the system's behavior, may present challenges in measuring entanglement. Its description of the system often involves mean-field approximations, which might not fully capture the entanglement present in the system, consequently, the Gutzwiller framework could be more intricate and less straightforward compared to MPS.

Moreover, MPS offers unique capabilities, allowing us to delve into systems of considerable size where thermodynamic properties become evident. This is in contrast to methods like exact diagonalization, renowned for their precision but impracticality for larger systems. Importantly, as we focus on 1D spin chains, it's worth noting that MPS methods seamlessly extend to 2D models[60] and are not restricted solely to systems involving spin-1 particles. This versatility underscores the broad applicability and relevance of MPS in diverse quantum systems[61;62;63].

In the realm of computational advantages, tensor networks, such as MPS, offer a significant breakthrough in dealing with the curse of dimensionality inherent in quantum many-body systems. Consider a spin-1 system, where the state is described by a vast number of coefficients, growing exponentially with the system's size. Traditional methods, like storing the full state, quickly become impractical due to this exponential growth.

Tensor networks address this challenge by parameterizing the state in terms of a polynomial number of parameters, achieved through the concept of bond dimension. The bond dimension acts as a cap on the entanglement between neighboring particles, effectively limiting the complexity of the description while retaining essential quantum correlations. By controlling the bond dimension, Tensor networks strike a balance between accuracy and computational feasibility, allowing for efficient representation and manipulation of quantum states.

Moreover, we say that tensor networks satisfies the entanglement entropy area law[22], if for every partition of it into two connected parts separated by a boundary ∂_L, the entanglement entropy is upper bounded by $S\partial_L \leq c|\partial_L|$, where c is some constant, independent of L. In other words, it means that the entanglement entropy of a subset of the system scales as the contact area of the subset with the rest of the system, rather than its volume, as in typical quantum states. This property reflects the inherent locality of quantum entanglement and plays a crucial role in the efficiency of TN algorithms.

To fully leverage the advantages of Matrix Product States, it is essential to understand the mathematical tools and construction principles underpinning this method. Two critical components in the effective application of MPS are the singular value decomposition (SVD) and the systematic building of MPS representations. In the following sections, we will dive into the role of SVD in simplifying and optimizing the tensor network structures, and explore the practical steps involved in constructing MPS representations.

4.2.1 | Singular Value Decomposition

A fundamental mathematical component in numerical algorithms applied to TNs involves the Singular Value Decomposition (SVD)[24], closely related with the Schmidt decomposition of quantum states. The Schmidt decomposition asserts the possibility of expressing a bipartite quantum state using an orthonormal correlated basis for the two parties, known as the Schmidt basis. This representation includes χ real and positive coefficients, referred to as the Schmidt coefficients, where χ is denoted as the Schmidt rank. When orthonormal bases for two vector spaces, let's say "A" and "B" are considered for the coefficients of the state vector representation, the Schmidt decomposition aligns with the SVD of the matrix containing these coefficients.

The Schmidt decomposition states that a bipartite quantum system $|\Psi\rangle_{AB} \in \mathcal{H}_A \otimes \mathcal{H}_B$ can always be written as:

$$|\Psi\rangle_{AB} = \sum_{\alpha=1}^{\chi} \lambda_\alpha |\alpha\rangle_A |\alpha\rangle_B, \qquad \text{with} \quad \{|\alpha\rangle_A\}, \{|\alpha\rangle_B\} \quad \text{orthonormal basis,} \tag{4.2}$$

where $\lambda_\alpha \geq 0$ are the Schmidt coefficients which are real numbers and $\chi \leq min(d_A, d_B)$ the Schmidt rank.

In terms of matrix components and its diagrammatic form (see figure 4.2), this reads:

$$|\Psi\rangle_{AB} = \sum_{ij} \Psi_{ij} |i\rangle_A |j\rangle_B; \qquad \text{where} \quad \Psi_{ij} = \sum_{\alpha\beta}^{\chi} U_{i\alpha} \Lambda_{\alpha\beta} V^\dagger_{\beta j} \tag{4.3}$$

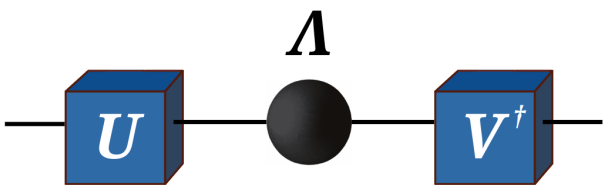

Figure 4.2: Diagrammatic form of the SVD where $\Lambda_{\alpha\beta} = \lambda_\alpha \delta_{\alpha\beta}$ are the Schmidt coefficients.

The key takeaway from this brief exploration is that the Schmidt decomposition for a quantum state aligns with the SVD for its coefficients when there exists an orthonormal basis for the Hilbert spaces $\mathcal{H}_{A/B}$. This observation holds significant implications for approximation strategies within TN methods. Specifically, truncating singular values is directly connected to truncating Schmidt coefficients, either precisely or approximately (especially in scenarios involving non-orthonormal bases for $\mathcal{H}_{A/B}$).

There exists a profound connection between the geometric configuration of a selected TN and the entanglement among distinct spins within the quantum many-body state it encapsulates. In the context of a quantum state denoted as $|\psi\rangle$, the Von Neumann entropy emerges as the quantum counterpart to classical entropy, encapsulating the information content associated with the entanglement patterns and is defined as[64;30],

$$S(\hat{\rho}) = -\text{Tr}\left[\hat{\rho} log \hat{\rho}\right], \tag{4.4}$$

where $\hat{\rho} = |\psi\rangle\langle\psi|$ is the quantum state density matrix. By employing the definition of Von Neumann entropy, the concept of entanglement entropy comes to the fore as a quantification of quantum correlations within a bipartite quantum system. Consider a partitioning of the quantum state $|\psi\rangle$ into two non-overlapping components, denoted as A and B. The entanglement entropy, characterizing the quantum entanglement between these distinct partitions, is expressed as:

$$S(\hat{\rho}_A) = \text{Tr}[\hat{\rho}_A log \hat{\rho}_A] = -\text{Tr}[\hat{\rho}_B log \hat{\rho}_B] = S(\hat{\rho}_B), \tag{4.5}$$

where $\hat{\rho}_A = Tr_B[\hat{\rho}]$ is the reduced density matrix of subsystem A and $\hat{\rho}_B = Tr_A[\hat{\rho}]$ is the reduced density matrix of subsystem B. The positive eigenvalues λ_α^2 of $\hat{\rho}_A$ and $\hat{\rho}_B$ correspond to the Schmidt values λ_α of the Schmidt decomposition of $|\psi\rangle$ into A and B parts respertively. This connection further extends to the truncation of entanglement within the quantum state, as evidenced by the entanglement entropy S between A and B: $S = -\sum_{\alpha=1}^{\chi} \lambda_\alpha^2 log \lambda_\alpha^2 \leq log \chi$[65].

4.2.2 | Building a MPS

In the previous section, we explored the intimate connection between the geometrical structure of TN and the upper bound imposed by the Schmidt rank. Exploiting this relationship unveils an interesting opportunity: we can intentionally choose TN representations for quantum states that naturally satisfy the entanglement entropy area law. These specifically crafted TN representations prove valuable for approximating quantum states found in nature, as these states often exhibit ad-

herence to the entanglement entropy area law[22;66].

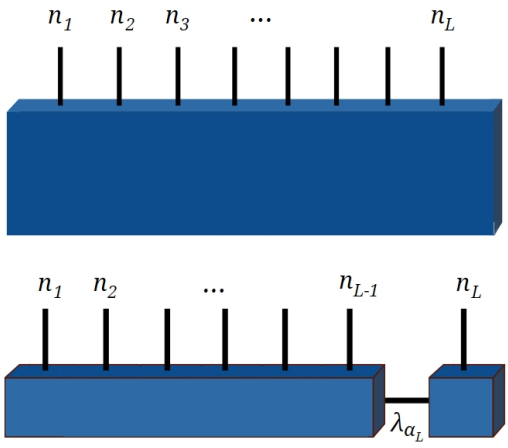

Figure 4.3: Decomposition of a tensor in terms of a MPS. Here the vertical legs correspond to the internal degrees of freedom or physical indexes (magnetic projections in this work), while the horizontal links λ (whose magnitude is χ) are the bonds between the tensors and their dimension given by the Schmidt rank.

Let's consider a system of N quantum particles, and the ket $|\psi\rangle$ that describes the state of the entire system. The state for the entire system is represented by vector in the Hilbert space $\mathcal{H}$, which is visualized as a tensor product of individual sites:

$$|\psi\rangle = \sum_{i_1,i_2,\ldots,i_L} C_{i_1,i_2,\ldots,i_L} |i_1\rangle \otimes |i_2\rangle \otimes \cdots \otimes |i_L\rangle, \tag{4.6}$$

where $C_{i_1,i_2,\ldots,i_L}$ is a tensor with N-legs (see Fig.4.3, top diagram) that represents the physical indexes of the system. The first step consists of performing a Schmidt decomposition to isolate one site from the rest of the chain splitting the system into two parts A and B,

$$|\psi\rangle = \sum_{\alpha}^{N_B} \lambda_\alpha |\alpha\rangle^A \otimes |\alpha\rangle^B. \tag{4.7}$$

Here $\{|\alpha\rangle^A\}$ and $\{|\alpha\rangle^B\}$ are two orthonormal bases corresponding to each part of the system, with N_A and N_B elements.

Before proceeding with the tensor splitting process, let's see how we would rewrite the above bases in terms of a suitable basis, which in second quantization formalism constitutes the occupation basis. The transformation involves only projecting the state of the single site (B block), such that the state in Eq. (4.7) can be rewritten as:

$$|\psi\rangle = \sum_{\alpha, n_L} \lambda_\alpha \underbrace{\Gamma_\alpha^{n_L} |\alpha\rangle}_{|\omega_{\alpha_L}\rangle} |n_L\rangle. \tag{4.8}$$

Where $\Gamma_\alpha^{n_L}$ are the matrix elements of the transformation and $|n_L\rangle$ the Fock basis elements. Next, we must concentrate on block A of our system and break it down again into two blocks by means of Schmidt's decomposition as shown in Fig.4.4(a).

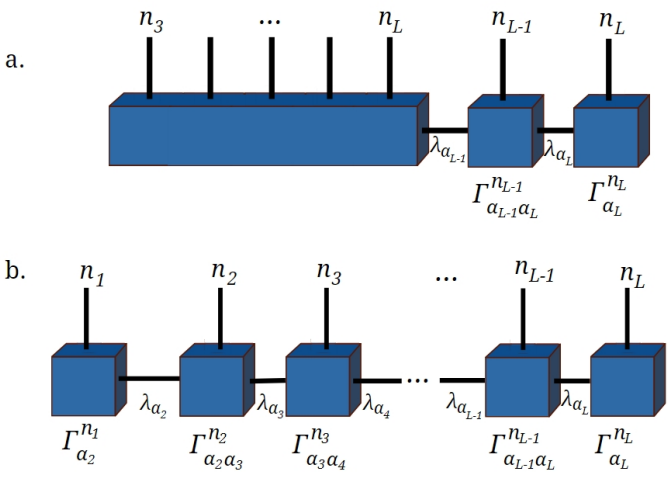

Figure 4.4: (a)Shows the next step of the decomposition for the site $L-1$. (b) Displays the completely decomposed state after iteratively applying the SVD on the blocks on the left.

$$|\alpha_L\rangle = \sum_{\alpha_{L-1}} \lambda_{\alpha_{L_1}} |\alpha_{L-1}\rangle |\omega\rangle, \tag{4.9}$$

same as for the first site that was separated, we projected on the Fock base the state $|\omega_{\alpha_L}\rangle$. Putting all the pieces together, the construction of the state takes the following form:

$$|\psi\rangle = \sum_{\substack{\alpha_{L-1}\alpha_L \\ n_{L-1}n_L}} \lambda_{L-1} \Gamma^{n_{L-1}}_{\alpha_{L-1}\alpha_L} \lambda_{\alpha_L} \Gamma^{n_L}_{\alpha_L} |\alpha_{L-1}\rangle |n_{L-1}\rangle |n_L\rangle, \tag{4.10}$$

being Ec.(4.8) the description of the state having separated only the last two sites of the whole chain. Continuing the same logic, the state of the whole system can be decomposed by separating all the sites one by one as showed on Fig. 4.3 and expressing them as:

$$|\psi\rangle = \sum_{\substack{\alpha_2 \dots \alpha_L \\ n_1 \dots n_L}} \Gamma^{n_1}_{\alpha_2} \lambda_{\alpha_2} \Gamma^{n_2}_{\alpha_2\alpha_3} \dots \lambda_{\alpha_{L-1}} \Gamma^{n_{L-1}}_{\alpha_{L-1}\alpha_L} \lambda_{\alpha_L} \Gamma^{n_L}_{\alpha_L} |n_1 \dots n_L\rangle, \tag{4.11}$$

Finally, it is possible to define a tensor $A^{n_s}_{\alpha_s\alpha_{s+1}} = \lambda_{\alpha_s} \Gamma^{n_s}_{\alpha_s\alpha_{s+1}}$. Such that in the end, the state written as an MPS takes the simplified form:

$$|\psi\rangle = \sum_{\substack{\alpha_2 \dots \alpha_L \\ n_1 \dots n_L}} A^{n_1}_{\alpha_2} A^{n_2}_{\alpha_2 \alpha_3} \dots A^{n_{L-1}}_{\alpha_{L-1} \alpha_L} A^{n_L}_{\alpha_L} |n_1 \dots n_L\rangle. \tag{4.12}$$

Here, the α_s are virtual indices that link a site to its neighboring sites and their dimension is closely related to the interlacing of the system, while the n_s correspond to the physical indices (internal degrees of freedom) that are given by the system under consideration. Taking into account Gutzwiller's ansatz as described in chapter 3, $|\psi\rangle = \prod_i \sum_{m_a, m_b} F^i_{m_a m_b} |m_a, m_b\rangle$, applying the above decomposition to rewrite the state in terms of a product of matrices we obtain the following,

$$|\psi\rangle_i = \otimes_i \sum_{m_a, m_b} f^{m_a}_{1,\alpha} f^{m_b}_{\alpha,1} |m_a, m_b\rangle, \tag{4.13}$$

showing explicitly the resemblance of the Gutzwiller ansatz and the MPS formulation, and hence, the fundamental essence of this work. In Eq.4.13 the bond dimension is given by α, which is nothing else than the dimension of the matrices, which define the entanglement between the states in the system. A large value of α, the representation better capture the entanglement in the system. And as discussed in Chapter 2 the Hamiltonian that governs the system under consideration, following the tight-biding approximation, fullfil this characteristic, and as a strong consequence the hopping term the Hamiltoniant term is retrived as the two-neighbouring sites contribution. Hence the whole system Hamitonian may be descomposed as two-sites Hamiltonians.

4.3 | Time-Evolving Block Decimation (TEBD)

The TEBD algorithm relies on an approximate representation of the state that is well-suited for one-dimensional quantum systems[67;68]. This representation selectively ignores highly entangled basis states, allowing for the efficient storage of low-energy states characterized by minimal bipartite entanglement. The algorithm introduces a method for applying operators that act on consecutive sites within this framework, facilitating the effective simulation of time evolution. This simulation is achieved by decomposing the time-evolution operator into sweeps of two-site gates through a Suzuki-Trotter expansion. TEBD is versatile, extending its capabilities to calculate ground states through the simulation of evolution in imaginary time.

4.3.1 | Suzuki-Trotter Decomposition

In numerous scenarios, calculating the exponential operator poses a considerable computational challenge. The conventional approach for evaluating the exponential operator e^{xM} involves diagonalizing the operator M. Yet, in quantum many body problems, the process becomes intricate, as the basis of the diagonalized representation is frequently nontrivial. This complexity arises from our

common interest in Hamiltonians featuring two or more terms that do not commute with each other.

The Suzuki Trotter decomposition is an approximation technique useful for simulating the time evolution of quantum systems in the context of quantum simulations. The decomposition is based on the Trotter-Suzuki formula, which states that for any two operators $\hat{A}$ and $\hat{B}$ that fulfills $[\hat{A}, \hat{B}] \neq 0$:

$$e^{\hat{A}+\hat{B}} = \lim_{n\to\infty} \left(e^{\frac{\hat{A}}{n}} e^{\frac{\hat{B}}{n}} \right)^n, \tag{4.14}$$

where the expansion is valid because for any two non-commutative operators the following approximation holds

$$e^{x\hat{A}} e^{x\hat{B}} = e^{x(\hat{A}+\hat{B})+\mathcal{O}(x^2)}. \tag{4.15}$$

The TEBD algorithm for simulating the time evolution of a 1D quantum state consists of using steps above by the application of time evolution operators between neighboring sites. This approach enables the efficient simulation of any moderately entangled one-dimensional state. The critical requirement is that the Hamiltonian must exclusively consist of next-neighbor terms, allowing it to be expressed as a sum over two-site Hamiltonians $\hat{H} = \sum_i^{N-1} \hat{H}_{i,i+1}$, here $\hat{H}_{i,i+1}$ is the Hamiltonian on the sites i and $i+1$. Such that,

$$\hat{H} = \sum_{i\ even} \hat{H}_{i,i+1} + \sum_{i\ odd} \hat{H}_{i,i+1} = \hat{A} + \hat{B}. \tag{4.16}$$

Then, we define the time evolution operator as $\hat{U}(\Delta t) = e^{-i\hat{H}_{i,i+1}\Delta t}$ (where we are choosing $\hbar = 1$). If we define $\tau \to -it$, we can perform an imaginary time evolution with $\hat{U}(\tau) = e^{-\tau\hat{H}}$ which allows us to find the ground state of a Hamiltonian, as we already did along the Chapter 3 using this same definition to calculate the Gutzwiller ground state. We need to express the evolution operator within the MPS formalism, which can be achieved through the Suzuki-Trotter Decomposition[69] as a product of individual next-neighbour evolution gates,

$$\hat{U}(dt) = \Big[\prod_{i\ odd} \hat{U}_{i,i+1}(dt) \Big] \Big[\prod_{i\ even} \hat{U}_{i,i+1}(dt) \Big], \tag{4.17}$$

where $\hat{U}_{i,i+1} \equiv e^{-i\hat{H}_{i,i+1}\Delta t}$ and acts on only two sites. This can be understood as follows: to do a single iteration of this operator, we first evolve the odd sites and then we evolve the even pair of sites. This is considered as a single iteration of the time evolution. Unlike Gutzwiller's method in which after each time step in the evolution process the state must be renormalized by hand, here it is handled implicitly through the structure of the algorithm rather than explicit renormalization at each step since the time evolution operator is unitary, hence keeps the norm of the state. The key step in TEBD where the MPS structure is restored involves SVD, followed by truncation of the smallest singular values. While the truncation introduces an approximation, the SVD itself decomposes the tensor

exactly into unitary matrices (up to the truncation): $A = U\Lambda V^\dagger$, where $U, V^\dagger$ are unitary matrices to the left and right, respectively and Λ is a diagonal matrix of singular values. After applying the SVD, the tensor is decomposed, and the smallest singular values are truncated. This truncation does introduce a small error[70], which can be seen as a slight deviation from perfect unitarity that can be controlled by choosing a sufficiently large bond dimension to capture the significant singular values while truncating only the smallest ones. Such that each SVD step ensures that the tensors remain normalized in a local sense.

4.3.2 | Update procedure

As in the previous section, our objective is to simulate time evolution through the repetitive application of evolution gates that act between neighboring sites in a Suzuki-Trotter decomposition. Unfortunately, these gates operate on two consecutive sites, leading to a partial disruption of the one-site translational invariance. Thus, we simply go one step further and expand to a two-site representation,

$$|\Psi\rangle = \sum_{\alpha\beta\gamma} \sum_{i} \lambda^i_\alpha \Gamma^i_{\alpha\beta} \lambda^{i+1}_\beta \Gamma^{i+1}_{\beta\gamma} \lambda^{i+2}_\gamma |m_i, m_{i+1}\rangle. \tag{4.18}$$

With the same symmetry argument used before, now assuming invariance by shifts of two sites, it follows that the state can be represented by Fig.4.5, which has a resemblance to equation 3.13 of Chapter3 where we broke down the state into two neighboring sites.

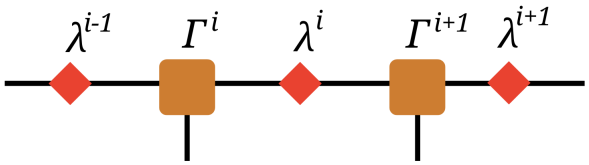

Figure 4.5: Initial trial two-sites state in terms of MPS showing explicitly the Schmidt coefficients and the corresponding transformation Γ to the occupation basis. *[Self made figure]*

Once we have prepared the initial trial state using the MPS representation with a two-site unit cell and incorporating the time evolution operator, we can employ the previously outlined approach to determine the variational ground state MPS, also shown in Figure 4.6.

We start the sequence by performing an imaginary time evolution over either even or odd pairs of sites, using the gate defined in red in Fig. 4.6 (a) and this is done through the contraction of the state with the operator U_{AB} (see Fig. 4.6 (b)). Subsequently a SVD is implemented (Fig. 4.6 (d))

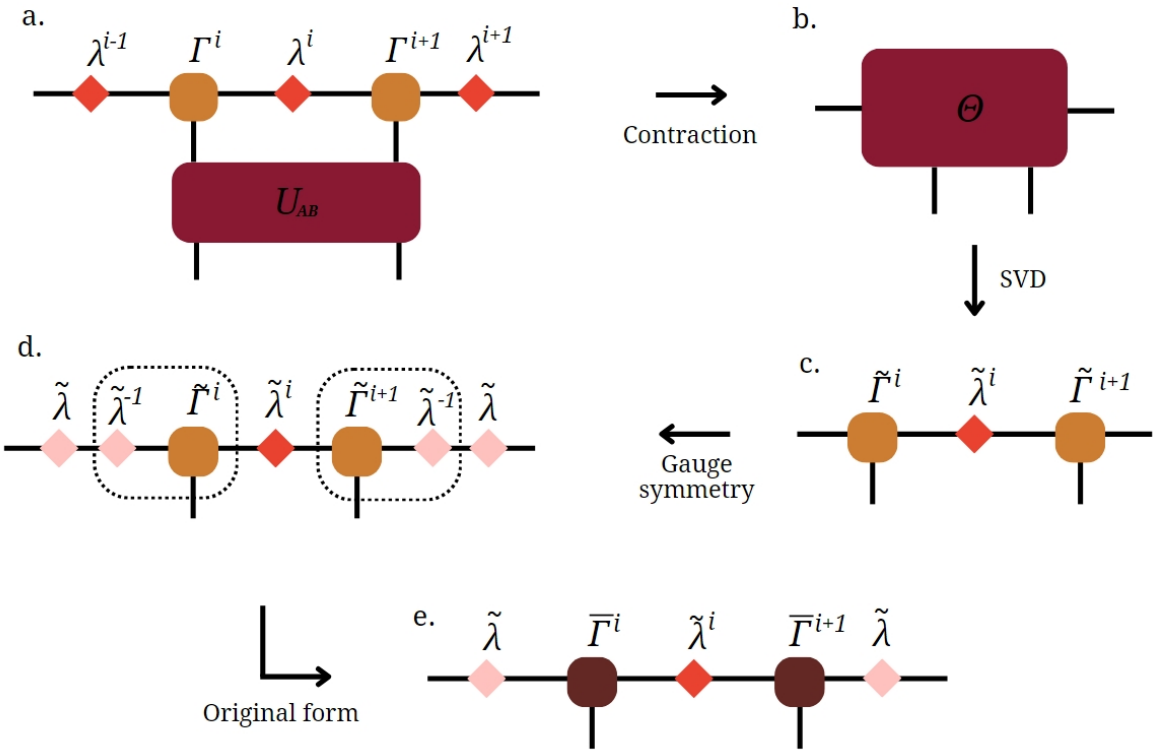

Figure 4.6: Logical sequence of execution of steps to perform a time evolution on the state.

to the evolved state to recover the canonical form of the MPS and carry out the truncation of the Schmidt coefficients to maintain the growth of the bond dimension stable. The final step consists of exploiting the Gauge symmetry of the system and introduce $\tilde{\lambda}\cdot\tilde{\lambda^{-1}}$ on both ends as showed in Fig. 4.6 (c) and absorbing the $\tilde{\lambda}^{-1}$ we obtain again the original form of the MPS, ready for the next evolution step. In addition to this processing, we are interested in monitoring the convergence of the energy after each time step to corroborate that the process is indeed finding the base state of the system.

4.3.3 | Python algorithm

The TEBD was implemented in Python using only the fundamental linear algebra libraries (numpy, math) following the existing example of an iTEBD implementation for the ising model in[71]. For this implementation a Victus HP laptop computer with AMD Ryzen 7 7840HS processor, 16 GB RAM and Ubuntu 24.04 LTS operating system was used.

The following are the detailed steps that structure the code and the different measurements that were performed in this work:

1. The first block of the code is composed of the definitions of the physical parameters (J, D, θ, N and χ), as well as the numerical parameters such as (τ : $timestep, iterations$). In addition, the Hamiltonian and the basic tensor contraction structures used throughout the code in more complex functions are also defined. For the purposes of this work, $N = 10$ sites were considered, $J = 1.0$ and the values of D and θ were varied according to the measurements shown in 4.4. The value of the bond dimension is not fixed *perse* but is calculated every time the SVD is performed, such that the truncation of the Schmidt coefficients does not entail much loss of information. Numerically speaking this is,

```
χ = np.min ([np.sum ( s > 1e-10 ), χ_max])
```

   On the other hand, τ is chosen such that the time step is small enough so the evolved state conserves its norm, and the number of steps the evolution is performed is giving by the convergence criteria of the energy $|E_i - E_f| < 10^-6$.
   Now, the canonical forms of an MPS are specific ways of representing these states such that certain properties, like normalization and orthogonality, are maintained. There are two types of canonical forms: the left-canonical form and the right-canonical form and their respective contractions are given by the functions (a) and (b) on Fig.4.7.

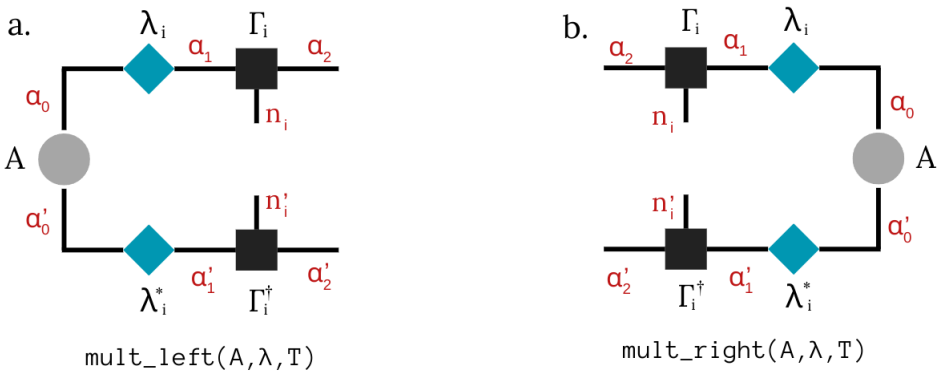

Figure 4.7: Scheme of the MPS contracted to the left and right respectively. Here A represents a tensor of dimension (χ, χ).

2. Once we have defined the ways of contracting the MPS we define the environment of a site i as the TN consisting of all the tensors in the original TN, except those at site i. Calculating the environments is crucial for the subsequent calculation of expected values of the observables,

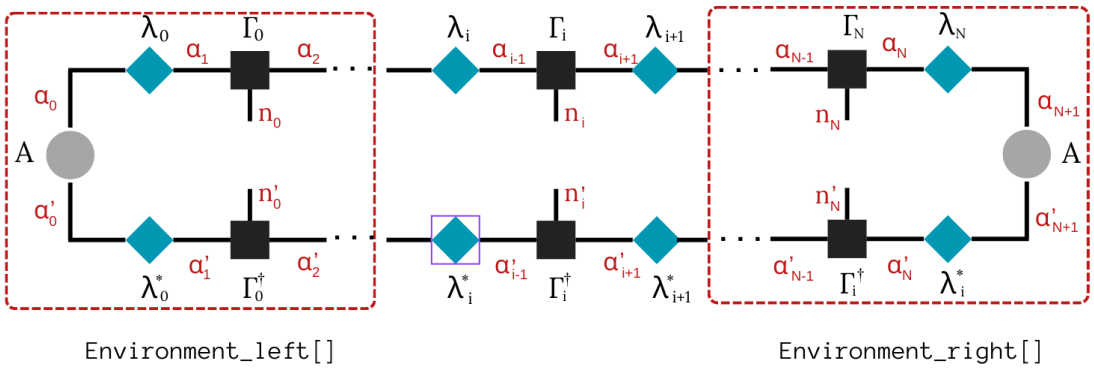

Figure 4.8: Schematic representation of the environment, where V in this case corresponds to the identity matrix.

where the left environment L_i for site i can be constructed recursively from the left-canonical tensors and similarly, the right environment R_i for site i can be constructed recursively from the right-canonical tensors starting with $L_1 = \mathbb{1}$ and $R_N = \mathbb{1}$.

3. After the whole structure has been built, which is entirely based on tensor contractions, it is necessary to perform some calculations of certain quantities. The most immediate and simple, but yet important, one concerns the calculation of the norm, for which we make a contraction between the ket and bra, for each site as shown in Fig.4.9(a). On the other hand, for the calculation of the expectation value of a two-sites observable we rather follow the scheme on Fig.4.9(b). It is worth to notice that this is valid for the Hamiltonian of our system since is a two-site and non-separable operator.

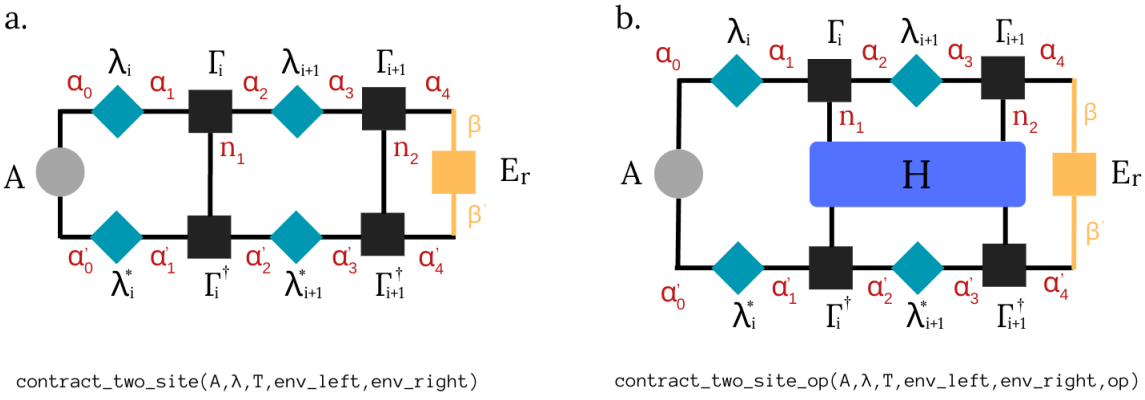

Figure 4.9: Contraction of the MPS for two consecutive sites with operator (b), and without operator (a). Here, V corresponds to the environment on the left, whatever it is and E_r corresponds to the right environment.

4. Once we figure how to compute the norm and the expectation value, we can now calculate the energy per site as shown in section 4.4 below:

$$E = \sum_i \frac{\langle \hat{H} \rangle}{\langle \psi | \psi \rangle} \Big/ L - 1. \tag{4.19}$$

Which is no more than incorporating diagrams (a) and (b) of Fig.4.9.

5. Using the same logic we can calculate other local observables as magnetization or density profiles and are introduced in the next section.

4.4 | Measurements

In this section we present the results of using the tensor network formalism, more specifically the MPS to represent a quantum many-body state and evolve it under the dynamics of an effective Hamiltonian. The previous sections have already explored how to write the state and how to evolve it through the TEBD. However, it is important to write explicitly how the operators are formulated in this formalism and how expected values are calculated for the purposes of the physical measurements made in this work.

Prior to studying the physical observables, it is worthwhile to verify an important feature of the system, namely entanglement. To do this, in Fig.4.10 two relevant quantities have been depicted, in a) the respective singular values for site 5 in each of the phases, in which it can be seen that for the first 20 values there is a significant decay, however, since the truncation of the Schmidt coefficients has a fairly high tolerance, the resulting vector has many components but of very small values. It can also be seen that the Ising and Dimer phases (blue and green lines, respectively) show more entanglement than the other phases. It is in fact the Dimer phase that shows the most entanglement with at least 3 orders of magnitude more than the next one. On the other hand, Fig.4.10 (b) shows the entanglement entropy that has been calculated as $S(A) = -\sum_i s_i^2 log(s_i^2)$, where s_i are the singular values obtained from the Schmidt decomposition across the bipartition between A and its complement B. This quantity exhibits a logarithmic growth, which is a great benefit for the use of MPS in 1D, as its controlled growth allows it to be used as a tool to determine to what extent the truncation of the Schmidt coefficients is leaving out relevant information.

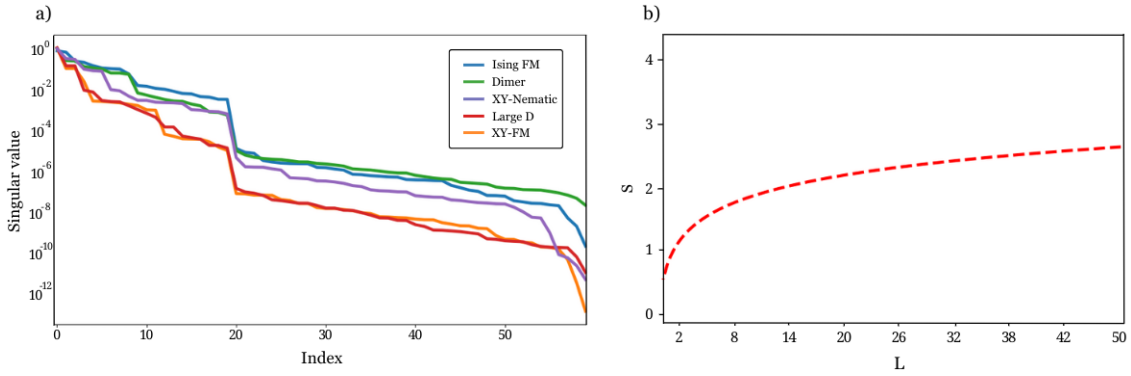

Figure 4.10: a) Shows the trend of the singular values for site 5 of the chain for each of the phases of the system (having considered a chain of 10 sites).(b) Scaling of the bipartite entanglement entropy S with the number of sites L.

4.4.1 | On-site observables

A huge advantage of the MPS representation of states is that only a few local matrices are needed to calculate the effect of a local operator on the state, or its expectation value. Here we look at the expectation value of a one-site operator $\hat{O}^i$ that acts only on the site i.

The expectation value is given by:

$$\langle\Psi|\hat{O}^i|\Psi\rangle = \sum_{\{n_i',n_i\}}\sum_{\{\alpha_i',\alpha_i\}} \langle n_1', n_2', ..., n_L'|\ldots\lambda^*_{\alpha_{i-1}}\Gamma^{i*}_{\alpha_{i-1},\alpha_i}\lambda^*_{\alpha_i}\ldots|\hat{O}^i|\ldots\lambda_{\alpha_{i-1}}\Gamma^{i}_{\alpha_{i-1},\alpha_i}\lambda_{\alpha_i}|n_1, n_2, ..., n_L\rangle, \quad (4.20)$$

in graphical representation, this becomes as shown as follows in Fig.4.11,

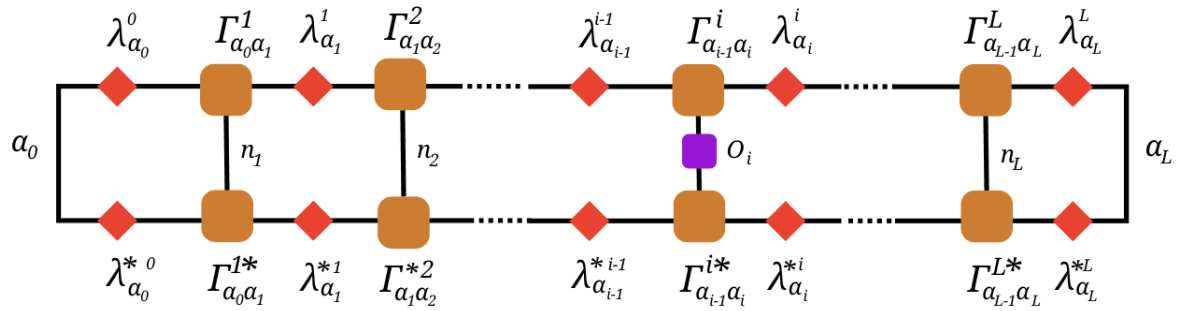

Figure 4.11: Scheme of the expectation value of a on-site operator $\hat{O}$, which is done by contracting the left and right environments along with the operator acting on the site i as showed on Fig. 4.8.

In Fig.4.11 notice the interior vertical lines, the projections n_i' from the bra and n_i from the ket meet. Due to the orthogonalization relation $\langle n_i'|n_i\rangle = \delta_{n_i',n_i}$ they have to be equal, except at the loca-

tion i. It is worth mentioning that all λ values are actually real, as they are singular values.

This expression can now be simplified by using the normalization Eq.4.24, which iteratively make all matrices from both ends of the chain all the way to site i contribute only with Kronecker deltas, such that the new scheme is as Fig.4.12. The remaining contribution can be seen as:

$$\langle\Psi|\hat{O}^i|\Psi\rangle = \sum_{n_i',n_i}\sum_{\alpha_i',\alpha_i}\langle n_i'|\lambda^*_{\alpha_{i-1}}\Gamma^{i*}_{\alpha_{i-1},\alpha_i}\lambda^*_{\alpha_i}|\hat{O}^i|\lambda_{\alpha_{i-1}}\Gamma^{i}_{\alpha_{i-1},\alpha_i}\lambda_{\alpha_i}|n_i\rangle \tag{4.21}$$

.

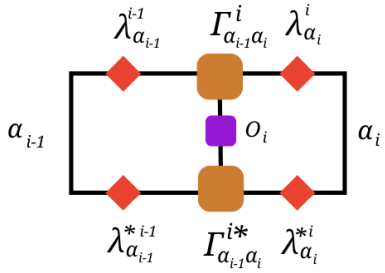

Figure 4.12: Reduced diagram of the expectation value for the operator $\hat{O}$ showed in Fig. 4.11.

Normalization

Considering the ansatz of the Eq. 4.12 to describe the system state, where each of the matrices $A^{n_s}_{\alpha_s\alpha_{s+1}}$ comes from an SVD and therefore satisfies:

$$\sum_{\alpha_L}\mathbb{A}^s\mathbb{A}^{\dagger s} = \mathbb{1}, \tag{4.22}$$

where the expression can be written in matrix components, this equation reads,

$$\sum_{\alpha_L}A^{\dagger n_s}_{\alpha_s,\alpha_{s+1}}A^{n_s}_{\alpha_s,\alpha_{s+1}} = \delta_{\alpha_i,\alpha_i'}, \quad \text{graphically:} \tag{4.23}$$

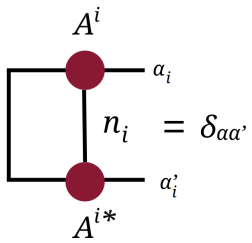

In the pictorial representation above, closed lines imply a summation. The normalization of the whole MPS can be deduced in a simple way, by applying the graphical form of Eq. 4.15 site by site. Along this work the state is written in the Canonical form such that the normalization becomes:

$$\sum_{n_i} (\Gamma^{n_i}_{\alpha_{i-1},\alpha})^\dagger (\lambda_\alpha)^2 (\Gamma_{\beta,\alpha_{i-1}}) = \mathbb{1}, \quad \text{graphically:}$$

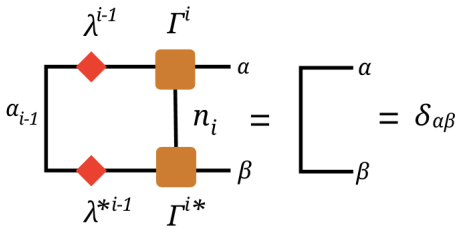

$$= \delta_{\alpha\beta} \tag{4.24}$$

A similar normalization can also be shown to hold when summing over the second matrix index of Γ^i and for the right side of the chain.

One of the peculiarities and differences of tensor networks with respect to the Gutzwiller ansatz is how the evolution of the system is handled by the TEBD algorithm. TEBD employs the Suzuki-Trotter decomposition to approximate the time evolution operator. This decomposition breaks the evolution into a series of short-time steps, allowing TEBD to handle the evolution more efficiently. Each short-time step is approximated by a sequence of local unitary operators, which act on a small number of neighboring sites in the quantum system. However, the evolution provided by TEBD is not perfectly unitary (see Fig. 4.13) due to the necessity of truncating the SVD at each step to manage the bond dimension. By carefully choosing an appropriate bond dimension and criteria for truncation, one can control the accuracy of the approximation, thereby minimizing the deviation from unitarity and preserving the norm of the state as closely as possible.

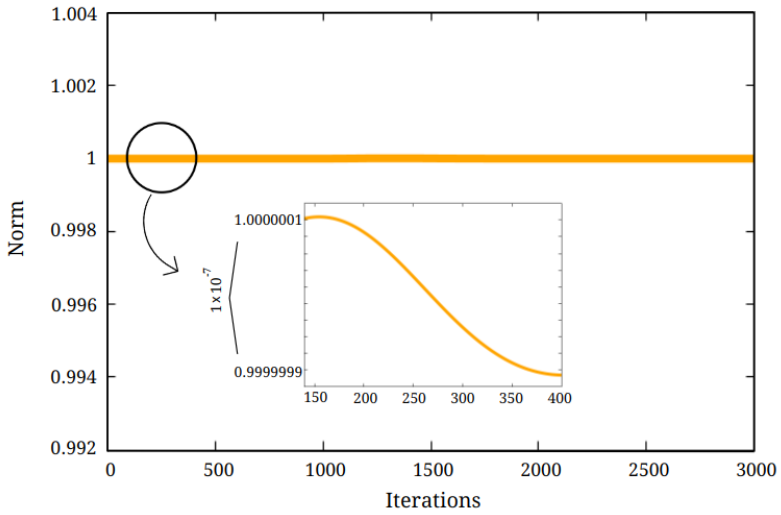

Figure 4.13: Norm of the state for each step during the process of imaginary-time evolution.

Fig.4.13 is performed for a chain of $L = 10$ sites with a time step $\tau = 0.001$ and $\chi = 20$. As can be seen at a scale of 1×10^{-1}, the norm remains constant at unity. However, zooming in proportionally

to 1×10^{-7} shows that the line has decaying behavior in sections, indicating that the unitary character of the TEBD is not absolute but is considerably good for the chosen parameters.

Energy and Magnetization profiles

For the calculation of the energy, the steps mentioned in Section 4.3.2 are carried out to make the respective contractions of the calculation for the expected value of the energy. As mentioned before, TEBD is particularly well-suited for simulating one-dimensional quantum systems because it leverages the structure of MPS, which efficiently represent the quantum state of 1D systems. This evolution is approximated using a Suzuki-Trotter decomposition to break the Hamiltonian into a series of local operators and then evolves it in imaginary time with the purpose of finding the ground state. Due to the fact that the use of Suzuki-Trotter decomposition introduces errors that accumulate over time the appropriate parameters such as the size of the time steps and the bond dimension χ (which controls the accuracy of the approximation), should be carefully chosen so that one can control the error introduced by the approximation.

Before plotting some values for the relevant parameters (D,θ), it is important to have in mind that introducing a quadratic Zeeman field alters the system's energy dynamics, leading to a partial lifting of its degeneracy. This alteration influences the preference for energy minimization among states characterized by different spin magnetic projections, depending on both the sign and strength of the field. In the absence of a quadratic term $(D = 0)$, the system exhibits triple degeneracy (see Fig. 4.14 b)), where states with magnetic projections of $-1, 0$, and 1 all minimize energy equally. Conversely, when $D \neq 0$, the degeneracy is modified: for $D < 0$, magnetic projections of -1 and 1 are equally favored, whereas for $D > 0$, projection 0 becomes the favored state (see Fig. 4.14a) and c)).

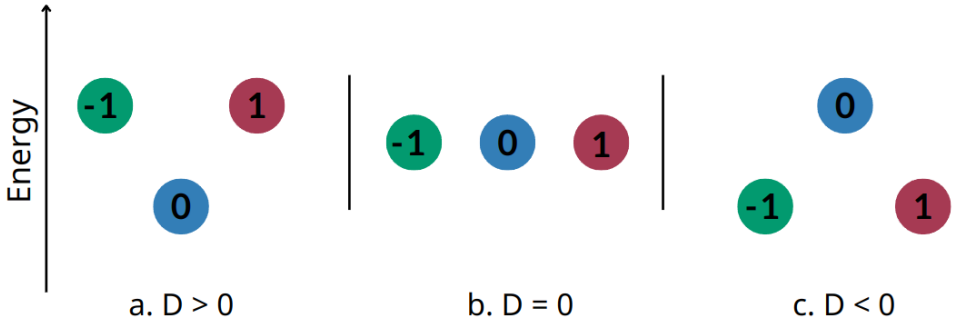

Figure 4.14: Diagram of the Zeeman field effect on magnetic projections. a) For $D > 0$ the minimization of the energy will be dominated by the 0 magnetic projection. b) For the case in which the Zeeman field is absent a triple degeneracy occurs and for c) $D < 0$ the magnetic projections $-1, 1$ are favored.

With this in mind, we refer back to the phase diagram shown in Fig. 2.3 of Chapter 2, which

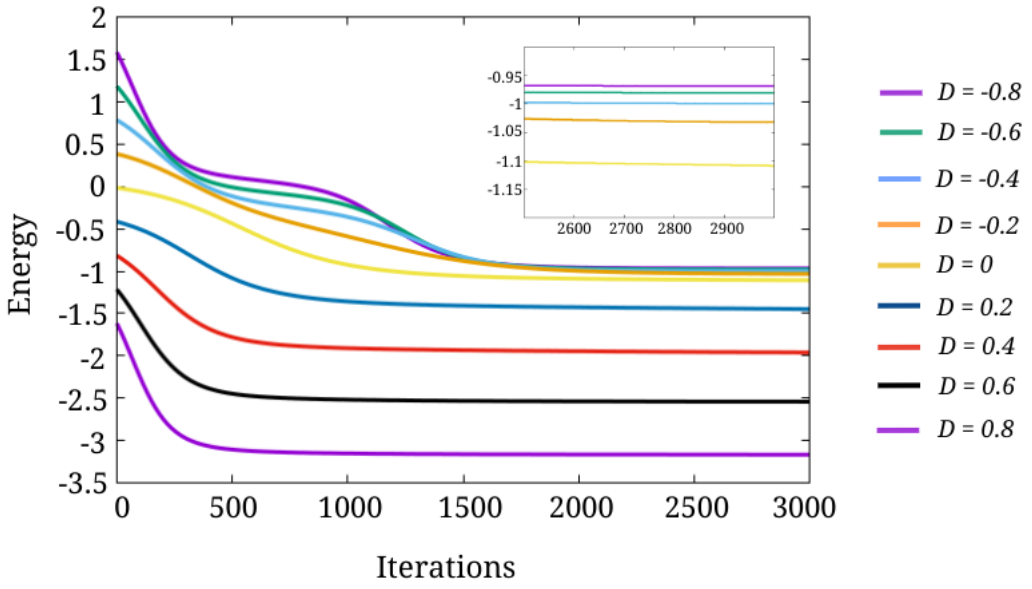

Figure 4.15: Convergence of the system energy across iterations for a value $\theta = -0.85$ varying the D field.

indicates for each pair of values of the interaction parameter θ and the quadratic magnetic field D in which phase of the system we are. To give us an idea of how the energy of the system behaves for a certain distribution of the relevant parameters, we plot the energy of the ground state for $\theta = -0.85$ and different values of the quadratic Zeeman field D, as showed in Fig.4.15.

It can be seen that the system converges to different energies for each value of the external field so that the energy has an inverse relationship with the quadratic field, where it becomes larger as D decreases. It can also be seen that the number of iterations varies for each case, with the Ising-FM being the region for which the energy converges the fastest, followed by XY-FM and then LargeD-FM.

The second measurement used to test the code corresponds to the magnetic density profiles, i.e., the percentage population of all magnetic spin projections per lattice site along the chain. This is an important measurement because it reports the known behavior of the system in each of the phases. For instance, Fig.4.16 (a) shows the XY-Ferromagnetic regime (visible for $-0.9\pi < \theta < -0.75\pi$ and $D < 0$) for which it is corroborated that for negative values of the Zeeman field, the spin magnetic population of $\sigma = 0$ dominates along the spin chain, this behaviour stays until a critical point D_c is detected, where a crossing line to the next phase is located (Fig4.16 (b)). The Ising-FM phase shows that the most dominant spin magnetic projections are $\sigma = \pm 1$, while the $\sigma = 0$ projection has a null contribution (see Fig.4.16 (c).), accounting for the expected behavior for that phase.

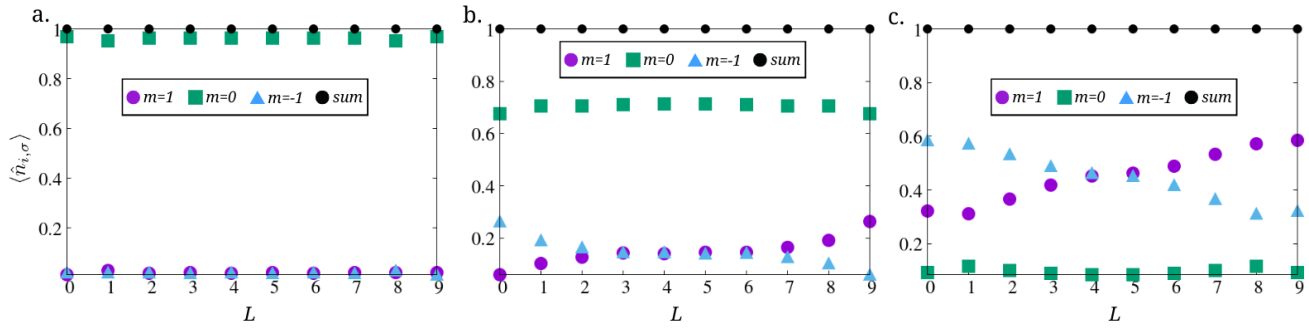

Figure 4.16: Magnetization profile for a system of $L = 10$ lattice sites and $\theta = -0.85\pi$. The plot a). corresponds to the XY-FM regime at $D = -0.4$, b). For $D = 0$ where the boundary to the next phase is located, it is not feasible to obtain a narrow result, and c). Ising-FM phase at $D = 0.4$.

A very similar analysis can be done for the plots in Fig. 4.17. This time $\theta = -0.7$ was taken, where for $D = -0.4$, the Large-D phase shows a dominance by the $\sigma = 0$ magnetic projection, while $\sigma = \pm 1$ present null contributions. Meanwhile, for the XY-Nematic phase ($D = 0.4$), the population of $\sigma = \pm 1$ are equall and dominant over $\sigma = 0$

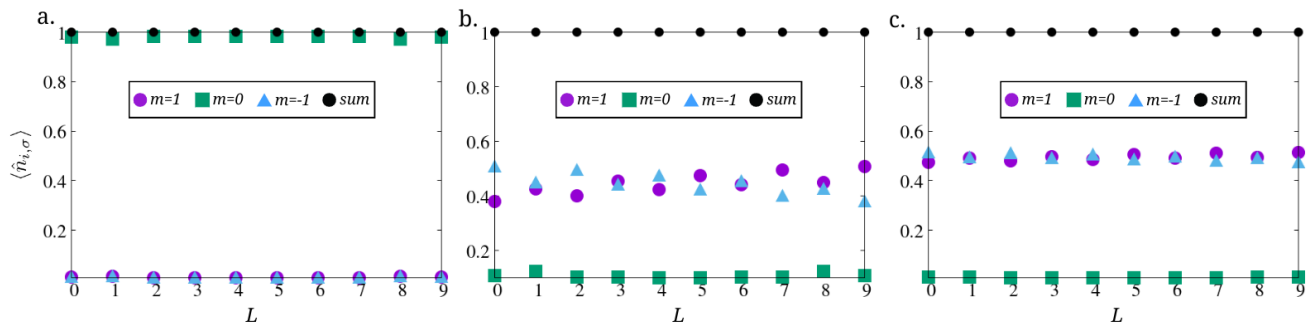

Figure 4.17: Magnetization profile for a system of $L = 10$ lattice sites and $\theta = -0.7\pi$. The plot a). corresponds to the Large-D phase at $D = -0.4$, b). shows the behaviour at a transition point and as in Fig. 4.16 is not very sharp, and c). shows XY-Nematic at $D = 0.4$.

Chirality

Chirality is one of the local observables that distinguishes between phases that are susceptible to the external quadratic Zeeman field. The expected value of the chirality in terms of the magnetization densities or spin operators is given by:

$$\frac{\langle\hat{\tau}\rangle}{L} = \frac{1}{L}\sum_i \langle\hat{\tau}_i\rangle = \frac{1}{L}\sum_i \langle\hat{n}_{i,m=-1} + \hat{n}_{i,m=1} - 2\hat{n}_{i,m=0}\rangle = \frac{1}{L}\sum_i \left\langle 3\left(\hat{S}_z^i\right)^2 - 2\hat{I}\right\rangle. \tag{4.25}$$

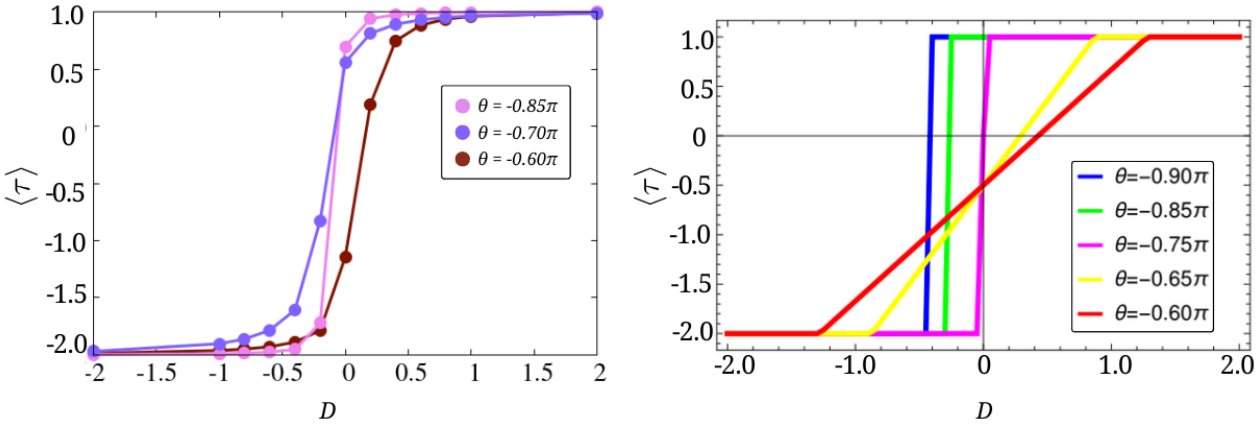

Figure 4.18: Chirality as a function of the external Zeeman field D for different values of θ. The image on the left corresponds to a measurement made using Tensor Networks, while the one on the right was made using the Gutzwiller ansatz [54].

This operator has information about the population difference between the two dominant magnetic varieties created by the external quadratic field. From the analysis of the magnetization profiles that characterized each phase and the eq. 4.25 it can be extracted that when $\langle\tau_i\rangle = -2$, the system is in the LargeD-FM regime, for $\langle\hat{\tau}\rangle = 1$ in the Ising-FM phase is present, and if $-2 < \langle\hat{\tau}\rangle < 1$ the XY-FM phase is the dominant. Also, from Fig. 4.18 it can be seen that for the Ferromagnetic side, the chirality reaches a minimum value when the field D takes values where the magnetic projection $m = 0$ grows. Then for $D > 0$ the chirality jumps to the maximum value denoting the domain of the $m \pm 1$ projections.

It is worth mentioning that the image generated using Gutzwiller was made with 50 sites, while the simulation used for TN only used $L = 10$ sites.

4.4.2 | Correlations

In addition to expected values of local operators discussed above, another type of observable, very important in physics studies, are correlation functions. As in the case of on-site observables all the matrices to the left/right of the interval in which the correlation takes place are reduced to the identity which notably simplify the numerical calculations. Let $\hat{\mathbb{O}}^i$ be some operator for which we

wish to compute the two point correlator $\langle \hat{\mathbb{O}}_1^i \hat{\mathbb{O}}_2^{i+\Delta} \rangle$ where the superscripts denotes the site at which the operator $\hat{\mathbb{O}}$ is applied. Graphically this expectation value is written as:

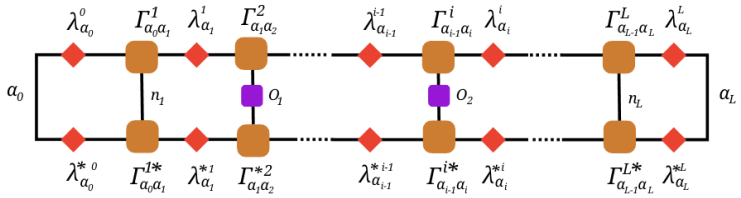

Figure 4.19: Scheme representing a two-point correlation, which is done by contracting the tensor train to the right/left of the sites where the operator is applied reducing it to 4.20.

We refer to the object

$$\mathbb{E}^i(\mathbb{O}^i) = \sum_{n_i, n_i'} \Gamma^{n_i'}_{\alpha_i', \alpha_{i+1}'} \mathbb{O}_{n_i', n_i} \Gamma^{n_i}_{\alpha_i, \alpha_{i+1}} \quad \text{graphically:}$$

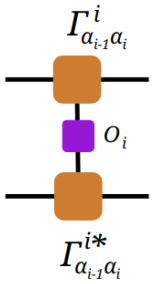

(4.26)

as the $\mathbb{O}$-transfer matrix. Note that we usually just refer to $\mathbb{E}_{\mathbb{1}}$ as the transfer matrix and simply denote it by $\mathbb{E}$. The correlator can then be written as:

$$\langle \mathbb{O}_1^s \mathbb{O}_2^{s+\Delta} \rangle = \mathrm{Tr}\Big[\mathbb{E}^s(\hat{\mathbb{O}}^s) \Big(\prod_{k=s+1}^{s+\Delta-1} \mathbb{E}^k(\mathbb{I}) \Big) \mathbb{E}^{s+\Delta}(\hat{\mathbb{O}}^{s+\Delta}) \Big], \tag{4.27}$$

and can be simplified as:

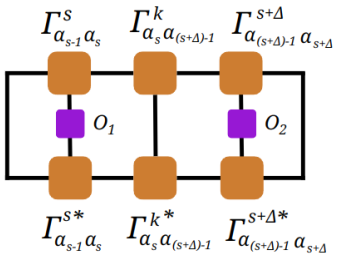

Figure 4.20: Reduced diagram to calculate a two-point correlation, where the trains of tensors on the edges and in between the sites where the operator $\mathbb{O}$ is acting, have been contracted

Correlation $\langle \hat{S}_i^z \hat{S}_j^z \rangle$

The correlation $\langle \hat{S}_i^z \hat{S}_j^z \rangle$ corresponds to a non-local measure and can be understood as an observable of two sites that can be separated as $\langle \hat{O}_{ij} \rangle = \langle \hat{\mathbb{O}}_i \otimes \hat{\mathbb{O}}_j \rangle$ and tells us how the z component of the spin is affected when it is in a certain projection at the i-th site by another one located at the j-th site.

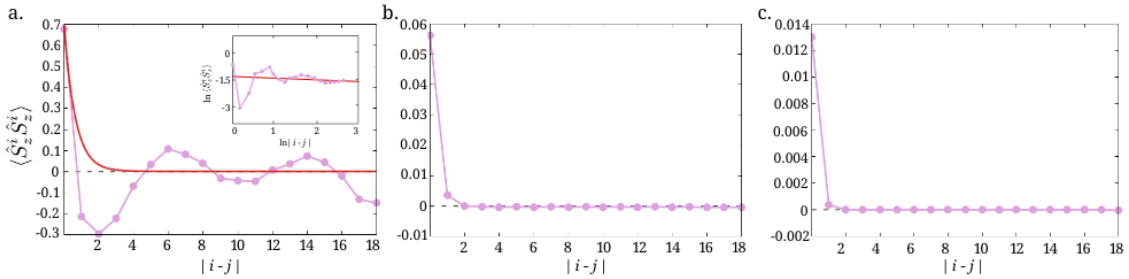

Figure 4.21: Correlation $\langle \hat{S}_z^i \hat{S}_z^j \rangle$ as a function of the distance between sites for a). Ising-FM at $\theta = -0.85\pi$ and D = 0.2, along with a log-log plot to showcase the algebraic decay b). XY-FM at $\theta = -0.85\pi$ and D = -0.2, c). at $\theta = -0.85\pi$ and D = -0.8 for LargeD-FM.

In the plots presented in Fig.4.21 it can be seen how much dependence there is between the spin magnetic projections along the lattice sites (in this case $L = 20$ has been taken). The plot contemplates the parameters $\theta = -0.85\pi$ and $D = 0.2; -0.2; -0.8$ corresponding to the three ferromagnetic phases. For all three a relatively fast decay of the correlation between the magnetic projection in the z-direction at site i-th and a different projection at site j-th can be seen.

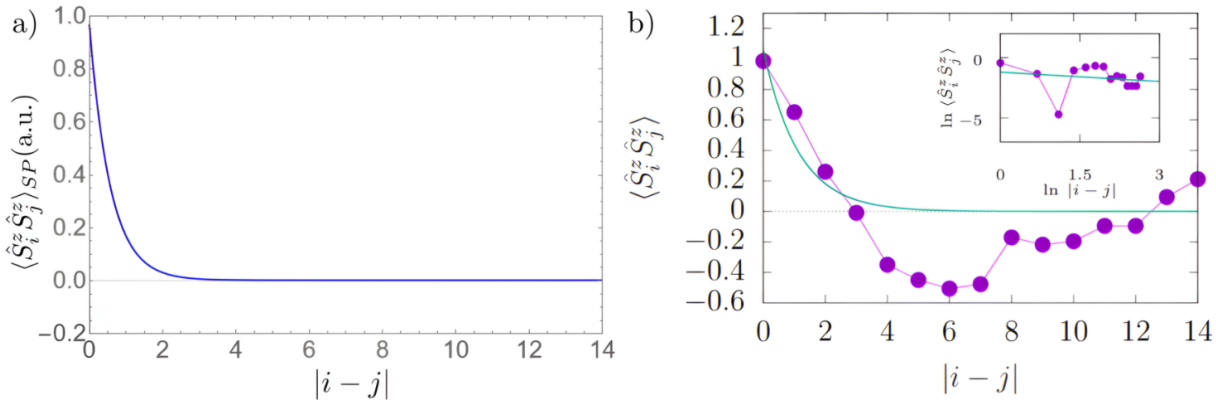

Figure 4.22: Plot taken from[72] where the correlation $\langle \hat{S}_i^z \hat{S}_j^z \rangle$ has been calculated as a function of the distance between the site, but on[72], a) is an analytical result obtained through a path integral formulation and b) numerical calculation using Quantum Monte Carlo[73].

After performing a log-log plot on the the behaviour on the correlation function for the Ising-FM regime (Fig.4.21), a linear relation arose, indicating that the curve is experiencing a decay shaped by a function like $y(x) = C \cdot x^{-a}$, where a is the slope of the linearized curve, which doesn't decay as quickly as quadratic or cubic relationships. This figure can be compared with the behavior observed in Fig.4.22 (a), where it can be seen the rapid decay of the correlation as one move away from the $i-th$ site is shown, but this time the result is obtained through an analytical procedure. In addition to this, the same correlations were measured by Diego Luis[73] (see Fig.4.22(b))for a similar set of parameters but this time the results were obtained through the implementation of a quantum Monte Carlo.

In spin-1 systems, in addition to the usual magnetic order parameters (like ferromagnetism or antiferromagnetism), we also have quadrupolar order parameters due to the higher-dimensional spin representation. Quadrupolar phases do not exhibit conventional magnetic order but rather involve alignments of quadrupole moments. These phases are characterized by the absence of dipolar magnetic order but can have nematic or other orders. In these phases, the order parameter is a rank-two tensor. A well-known example of a quadrupolar state is the $\hat{S}_z = 0$ state of a spin-1 system, which has no net magnetization but exhibits anisotropic spin fluctuations that break the $SU(2)$ symmetry[74]. The phases in spin-1 systems can be mapped out using models such as the bilinear-biquadratic Hamiltonian treated here, which considers both bilinear (spin-spin) and biquadratic (quadrupole-quadrupole) interactions. This model helps in understanding the competition between magnetic and quadrupolar degrees of freedom and in identifying different phases depending on the parameters of the system. From the measurement of the populations of spin-1 magnetic projections $(-1, 0, 1)$ in 4.16 and 4.17, an analysis can be done to gain insights into the quadrupolar characteristics of the system. For instance, the relative populations of the $\sigma = -1, 0, 1$, and states can indicate the presence of quadrupolar order. A high population of the $S_z = 0$ state often suggests quadrupolar characteristics since it represents a state with no net magnetization but potential quadrupolar order.

Additionally, MPS demonstrated advantageous performance in visualizing correlation effects, which are inherently present in quantum many-body systems. By employing the TEBD algorithm, we efficiently simulated our system of interest, reaching the ground state and obtaining accurate energy calculations and magnetization profiles. The MPS approach provided a straightforward and effective means of measuring entanglement entropy, enabling a detailed understanding of the system's quantum correlations. Furthermore, MPS required significantly fewer sites ($N = 10$) to achieve results comparable to the Gutzwiller ansatz with a larger number of sites (50 sites for the one-site Gutzwiller). This reduction in computational resources underscores the efficiency of the MPS method as well.

5 Conclusions and Perspectives

5.1 | Conclusions

Along this work we looked into the behavior of spin-1 bosons on a one dimensional lattice. Our study began by identifying the relevant components of the spin-1 Hamiltonian, which includes a general pseudopotential interaction among spinor particles and the influence of an external quadratic Zeeman magnetic field to get access to distinctive features, such as quadrupole magnetic modes and the potential for diverse phase transitions. These systems can exhibit collective magnetic behaviors, including ferromagnetic and antiferromagnetic phases, as well as more intricate structures when dipolar interactions are present. Likewise, the inclusion of a non-zero spin introduces additional dimensions to the interaction dynamics and the coupling with external magnetic fields. After determining the different regimes of the system, we applied perturbation theory to derive an effective Hamiltonian for the Mott insulator phase. This led to the bilinear-biquadratic Heisenberg model, which also incorporates the effects of the quadratic Zeeman field.

The project's primary goal was to explore the feasibility and effectiveness of translating the problem into the tensor network framework. This involved the careful study of a robust numerical method such as tensor networks, by means of which we found a way to represent our system based on MPS already existing in the literature and adapt them to the parameters of the system of interest. Subsequently, the approach was validated by comparing the results with those obtained with the traditional Gutzwiller method. The comparison aimed to ensure that the tensor network methods provided reliable and accurate results, thus establishing a solid foundation for future research using these advanced numerical techniques.
The methods employed in this study involved two primary approaches: the Gutzwiller variational ansatz and Tensor Network methods, specifically Matrix Product States (MPS). The Gutzwiller approach, both in its one-site and two-site forms, deals with the problem by solving a set coupled differential equations to determine the ground state phases, focusing on specific observables essential

for understanding the system's behavior. The drawback of this is that wanting to consider an ansatz with two coupled sites makes the size and complexity of the treatment of the differential equations to grow significantly. In contrast, the MPS method leverages the algebraic properties of tensor networks to efficiently characterize quantum systems. Utilizing the Time-Evolving Block Decimation (TEBD) algorithm which integrates the same imaginary time evolution used for the Gutzwiller, but this time accompanied by a Suzuki-Trotter decomposition. The MPS provides a compact representation of the quantum state, enabling accurate measurement of observables and offering insights into the system's phases. This dual-method approach ensured a comprehensive analysis and comparison of the numerical results, validating the effectiveness of tensor networks in representing and analyzing quantum many-body systems.

We dedicated a part of our investigation to the entanglement properties of these systems. In gapped systems, the number of significant singular values and their decay rate tend to obey an area law, where the entanglement entropy remains constant with increasing subsystem size. This property is particularly evident in gapped 1D systems, such as the Mott regime, where the calculated entanglement entropy varied slowly as a function of the subsystem size.

Through our analysis of the energy and magnetization profiles, we observed distinct physical properties that characterize the ground state of spin-1 bosons on a lattice. The ground state energy calculations revealed that the Tensor Network methods provided accurate and reliable results, closely matching those obtained from the Gutzwiller ansatz. This agreement validates the effectiveness of tensor network methods in capturing the essential physics of the system.

From the side of the physical measurements, we can highlight some concluding remarks from Chapter 4. Firstly, we retrieved the ground state of the system, which allowed us to measure the energy and corroborate that it converges for different values of the interaction parameter and external magnetic field, and the values are independent of the initial conditions for the coefficients. Subsequently, the magnetic profiles were obtained using the expected value of the magnetic spin projection per site, after evaluate the populations for different pair of parameter across the phase space, we could determine that for the Ising-FM and XY-Nematic phases (this is $D > 0$), the spin projections ± 1 have the highest population over the lattice, while projection 0 is almost null. Also, the magnetic spin projection 0 is dominant in the Large-D phase, as well as in the XY-FM, while there is a negligible contribution of the projections ± 1. All this is telling us that the magnetization profiles showed that the system exhibits various magnetic phases depending on the interaction parameters and the external magnetic field. Following this analysis, the next local observable measured is the chirality, for which in the Ising-FM region ($\theta = -0.85\pi, D = 0.5$) is $\tau = 0.997$, in a good agreement with the theoretical calculation given by 4.25. For the Large-D phase, the chirality is $\tau = -1.72$

which is close to the algebraic value $\tau = -2$ and coincides with the previous conclusion that the dominant manifold is the spin projection $\sigma = 0$. The chirality in the XY-FM phase is $\tau = -1.67$, so that is located in between the other two values from the other two phases interpreted as a competition between manifolds, with a dominance of the 0 magnetic spin projection.
The last observable we measure, was a non-local one as the correlation of the spin projections per site to study the magnetic dependence, evidencing an algebraic decay for almost all of the phases. This result is in agreement with two other measurements done by *Montilla* and *Gonzalez* in the framework of their bachelor's thesis, where they also calculated this observable by developing an analytical functional method such as Green's functions and path integrals, and a numerical method such as quantum Monte Carlo, respectively.
This work introduces a numerical perspective, contained in the world of tensor networks, that allows to approach models that are frequently used in the Solid State research group of the Universidad del Valle and that has qualities that can be useful to reach corners that are not reachable with other numerical methods, leaving the door open to continue undermining in the different tools that this formalism offers.

5.2 | Perspectives

This work was intended to introduce a tool that would provide a reformulation of quantum many-body systems that would facilitate their numerical implementation when the traditional derivation of differential equations becomes too complex. However, the world of tensor networks comprises many structures, each with their respective properties suitable for different types of systems, which deserve to be explored further. Therefore, as perspectives of this work it is considered appropriate:

- To build a translationally invariant MPS which allows to apply an iTEBD (infinite time-evolving block decimation) which at the same time allows to simulate unitary evolution and to compute the ground state of one-dimensional quantum lattice systems in the thermodynamic limit. Here the algorithm would be extended to tackle a much broader class of problems. Namely, the study of gapless systems allowing for the exploration of the magnetic properties of our system of interes but this time in the superfluid regime.

- Perform the numerical implementation of the the two-sites extension of the Gutzwiller ansatz and compare its results with those obtained from the Tensor Network method to compare the amount of computational resources used and to know in terms of accuracy and ease of implementation, what are the advantages and limitations of each method.

- Reformulate the problem in terms of other more adequate bases to study the physics of the system that allow to explore more clearly the properties displayed by the quadrupole degree of

freedom. An example of this could be to reformulate the whole problem in terms of the basis of spin-coherent states or the cartesian basis, in such a way as to separate the bilinear-biquadratic Hamiltonian into contributions where the quadrupole can be made independent.

- Regarding the physics of the system, it is worthwhile to exploit the entanglement properties of the MPS structure and to navigate in the dimer phase that has been little explored in recent works, as well as to analyze useful parameters that allow us to describe some of the physics at the $D = 0$ phase transition line, for which no relevant information could be extracted in the measurement performed in this work.

A Effective Hamiltonian

This appendix outlines the computations that led to deriving the effective Hamiltonian for the Mott insulator. This derivation involves applying second-order quasi-degenerate perturbation theory to the kinetic term of the Bose-Hubbard Hamiltonian for spin-1 particles. The section concludes by obtaining the bilinear biquadratic Heisenberg Hamiltonian.

A.1 | Second Order Perturbation Theory

Van Vleck's quasi-degenerate perturbation theory aims to iteratively reconfigure the Hamiltonian matrix into an effective Hamiltonian that is block diagonal. By employing similarity transformations in this process, the resulting effective Hamiltonian shares identical eigenvalues with the original matrix[75].

The theory is particularly useful when dealing with systems that exhibit degeneracy, where two or more states have the same energy. Van Vleck's approach is designed for situations where the degeneracy is not exact but is instead lifted by a perturbation, and there is a small energy separation between the nearly degenerate states. The total Hamiltonian of the system is considered the sum of a zeroth-order Hamiltonian (whose solutions are known) and a perturbation Hamiltonian, which is responsible for lifting the degeneracy.

$$\hat{H} = \hat{H}_0 + \hat{V}, \tag{A.1}$$

here, $\hat{H}_0$ is the unperturbed Hamiltonian, and $\hat{V}$ is the perturbation. In our case, we will use the kinetic term of the spin 1 Bose Hubbard Hamiltonian as the perturbation. Before the application of perturbation theory, we must first diagonalize the unperturbed Hamiltonian,

$$\begin{aligned}\hat{H}_0 = \sum_i \frac{g_2}{2}\Big(\hat{b}_1^\dagger \hat{b}_1^\dagger \hat{b}_1 \hat{b}_1 + \hat{b}_{-1}^\dagger \hat{b}_{-1}^\dagger \hat{b}_{-1} \hat{b}_{-1} + 2\hat{b}_1^\dagger \hat{b}_0^\dagger \hat{b}_1 \hat{b}_0 + 2\hat{b}_{-1}^\dagger \hat{b}_0^\dagger \hat{b}_{-1} \hat{b}_0\Big) + \frac{g_0 + 2g_2}{6} \hat{b}_0^\dagger \hat{b}_0^\dagger \hat{b}_0 \hat{b}_0 \\ + \frac{g_2 - g_0}{3}\Big(\hat{b}_1^\dagger \hat{b}_{-1}^\dagger \hat{b}_0 \hat{b}_0 + \hat{b}_0^\dagger \hat{b}_0^\dagger \hat{b}_1 \hat{b}_{-1}\Big) + \frac{2g_0 - g_2}{3} \hat{b}_1^\dagger \hat{b}_{-1}^\dagger \hat{b}_{-1} \hat{b}_1 \\ - \mu \sum_{i,\sigma} \hat{n}_{i\sigma} + Q \sum_{i,\sigma} \sigma^2 \hat{n}_{i,\sigma},\end{aligned} \tag{A.2}$$

where we have the terms associated to the interaction between the particles, the chemical potential and the quadratic Zeeman field.
First, let's write the states in a more convenient way,

$$|S, m, n\rangle \quad = \quad |1, m, n\rangle \quad = \quad |m, n\rangle,$$

where S is the total spin, m is the quantum number associated with the magnetic projections, and n is the number of particles. Here, we already know the three values the quantum number m can take:

$$|-1, n_{-1}\rangle \otimes |0, n_0\rangle \otimes |1, n_1\rangle \quad = \quad |n_{-1}\rangle \otimes |n_0\rangle \otimes |n_1\rangle.$$

Once defined the form of the states we are going to consider the easiest case which corresponds to two sites and two particles inside, such that we can define virtual and target states as shown in the table below, where each ket is labeled with a subscript pointing to its respective site.

$\|100\rangle_1 \otimes \|100\rangle_2$	$\|200\rangle_1 \otimes \|000\rangle_2$
$\|100\rangle_1 \otimes \|010\rangle_2$	$\|020\rangle_1 \otimes \|000\rangle_2$
$\|100\rangle_1 \otimes \|001\rangle_2$	$\|002\rangle_1 \otimes \|000\rangle_2$
$\|010\rangle_1 \otimes \|100\rangle_2$	$\|110\rangle_1 \otimes \|000\rangle_2$
$\|010\rangle_1 \otimes \|010\rangle_2$	$\|101\rangle_1 \otimes \|000\rangle_2$
$\|010\rangle_1 \otimes \|001\rangle_2$	$\|011\rangle_1 \otimes \|000\rangle_2$
$\|001\rangle_1 \otimes \|100\rangle_2$	
$\|001\rangle_1 \otimes \|010\rangle_2$	
$\|001\rangle_1 \otimes \|001\rangle_2$	

Calculating the energy for the virtual states is easy in this case because since we only have one particle in each site we don't need to deal with the interaction term of the Hamiltonian, but only with the chemical potential and quadratic Zeeman field. However, for the target states, we do have

interaction since there are now two particles in the same site. It is worth noting that two target states are not diagonal,

$$\begin{aligned}\hat{H}_0|020\rangle &= \left[-2\mu + \frac{2g_2+g_0}{6}\right]|020\rangle + \frac{\sqrt{2}}{3}(g_2-g_0)|101\rangle \\ \hat{H}_0|101\rangle &= \left[-2\mu + 2Q + \frac{g_2+2g_0}{3}\right]|101\rangle + \frac{g_2-g_0}{3}\sqrt{2}|020\rangle\end{aligned} \tag{A.3}$$

Collecting all the information together,

Virtual states	Energy
$\|200\rangle\otimes\|000\rangle$	$-2\mu+2Q+g_2$
$\|020\rangle\otimes\|000\rangle$	Non-diagonal state
$\|002\rangle\otimes\|000\rangle$	$-2\mu+2Q+g_2$
$\|110\rangle\otimes\|000\rangle$	$-2\mu+Q+g_2$
$\|101\rangle\otimes\|000\rangle$	Non-diagonal state
$\|011\rangle\otimes\|000\rangle$	$-2\mu+Q+g_2$

The following task is diagonalize the matrix associated to the subspace spanned by $|020\rangle|000\rangle$ and $|101\rangle|000\rangle$.

$$\begin{array}{c} \\ \langle 101| \\ \langle 020| \end{array}\begin{array}{c} \begin{array}{cc} |101\rangle & |020\rangle \end{array} \\ \begin{bmatrix} 2Q+\frac{g_2+2g_0}{3} & \frac{\sqrt{2}}{3}(g_2-g_0) \\ \frac{\sqrt{2}}{3}(g_2-g_0) & \frac{2g_2+g_0}{3} \end{bmatrix} \end{array} \tag{A.4}$$

From the characteristic equation, the eigenvalues and eigenstates,

$$\lambda_\pm = Q + \frac{(g_0+g_2)}{2} \pm \frac{1}{2}\sqrt{4Q^2 + \frac{4}{3}Q(g_0-g_2) + (g_0-g_2)^2}. \tag{A.5}$$

The eigenstates are going to be a superposition of the non-diagonal states,

$$\begin{aligned}|+\rangle &= A|101\rangle + B|020\rangle \\ |-\rangle &= C|101\rangle + D|020\rangle.\end{aligned}$$

The constants can be found from $\hat{H}_0|\pm\rangle = \lambda_\pm|\pm\rangle$,

$$\frac{B}{A} = \frac{\lambda_+ + 2Q - (g_2+2g_0)/3}{\sqrt{2}(g_2-g_0)/3}, \tag{A.6}$$

where, $\langle 101|+\rangle = A$ and $\langle 020|+\rangle$. And due to the orthogonality $\langle -|+\rangle = 0$, we can find C and D as $-B/A = C/D$. Now, parametrizing $|+\rangle$ and $|-\rangle$,

$$|+\rangle = \cos\theta\,|101\rangle + \sin\theta\,|020\rangle, \qquad |-\rangle = -\sin\theta\,|101\rangle + \cos\theta\,|020\rangle. \tag{A.7}$$

Where,

$$\tan\theta = \frac{\lambda_+ - 2Q - (g_2 + 2g_0)/3}{\sqrt{2}(g_2 - g_0)/3}. \tag{A.8}$$

From here, the idea is try to use Quasi-Degenerate Perturbation Theory to add the hopping as a perturbation. The matrix representation of the effective Hamiltonian up to a second order correction are given by the expression A.9:

$$H^{(2)}_{mm'} = \frac{1}{2}\sum_l \langle m|H_t|l\rangle\langle l|H_t|m'\rangle\left[\frac{1}{E_m - E_l} + \frac{1}{E'_m - E_l}\right], \tag{A.9}$$

where m, m' are the target states and l are the virtual ones. The effect of the hopping term over the target states can be condensed in the following table,

Target states		Virtual states	
m	E_m	l	E_l
$\|100\rangle\|100\rangle$	$-2\mu + 2Q$	$\|200\rangle\|000\rangle$	$-2\mu + 2Q + g_2$
$\|100\rangle\|010\rangle$	$-2\mu + Q$	$\|+\rangle\|000\rangle$	$-2\mu + \lambda_+$
$\|100\rangle\|001\rangle$	$-2\mu + 2Q$	$\|002\rangle\|000\rangle$	$-2\mu + 2Q + g_2$
$\|010\rangle\|100\rangle$	$-2\mu + Q$	$\|110\rangle\|000\rangle$	$-2\mu + Q + g_2$
$\|010\rangle\|001\rangle$	-2μ	$\|-\rangle\|000\rangle$	$-2\mu + \lambda_-$
$\|010\rangle\|001\rangle$	$-2\mu + Q$	$\|110\rangle\|000\rangle$	
$\|001\rangle\|100\rangle$	$-2\mu + 2Q$		
$\|001\rangle\|010\rangle$	$-2\mu + Q$		
$\|001\rangle\|001\rangle$	$-2\mu + 2Q$		

The matrix representing the effective Hamiltonian corresponds to a matrix of 81 terms but only a few terms are non-zero, and taking into account some constraints, we can reduce the calculation to only 5 terms. On one hand, we have that the Hamiltonian is hermitic such that it is only necessary to calculate the upper or lower triangle, moreover, there is an exchange symmetry between the states of the sites, such that $H_{2i} = H_{4i}$, $H_{3i} = H_{7i}$ and $H_{6i} = H_{8i}$.

$$
\begin{aligned}
H_{11} &= 4t^2\left(\frac{1}{E_1 - E_{l_1}}\right) = \frac{-4t^2}{g_2}, \\
H_{22} &= 2t^2\left(\frac{1}{E_2 - E_{l_4}}\right) = \frac{-2t^2}{g_2}, \\
H_{33} &= 2t^2\left(\frac{cos^2\theta}{2Q - \lambda_+} + \frac{sin^2\theta}{2Q - \lambda_-}\right) = 2t^2\Delta, \\
H_{55} &= -4t^2\left(\frac{sin^2\theta}{\lambda_+} + \frac{cos^2\theta}{\lambda_-}\right) = 4t^2\Omega, \\
H_{53} &= \sqrt{2}t^2 sin\theta cos\theta\left(\frac{1}{2Q - \lambda_+} - \frac{1}{2Q - \lambda_-} - \frac{1}{\lambda_+} + \frac{1}{\lambda_-}\right) = \sqrt{2}t^2\xi.
\end{aligned}
$$

The Hamiltonian in its matrix form is:

$$
H^{(2)} = \begin{pmatrix}
\frac{-4t^2}{g_2} & 0 & 0 & 0 & 0 & 0 & 0 & 0 & 0 \\
0 & \frac{-2t^2}{g_2} & 0 & \frac{-2t^2}{g_2} & 0 & 0 & 0 & 0 & 0 \\
0 & 0 & 2t^2\Delta & 0 & \sqrt{2}t^2\xi & 0 & 2t^2\Delta & 0 & 0 \\
0 & \frac{-2t^2}{g_2} & 0 & \frac{-2t^2}{g_2} & 0 & 0 & 0 & 0 & 0 \\
0 & 0 & \sqrt{2}t^2\xi & 0 & -4t^2\Omega & 0 & \sqrt{2}t^2\xi & 0 & 0 \\
0 & 0 & 0 & 0 & 0 & \frac{-2t^2}{g_2} & 0 & \frac{-2t^2}{g_2} & 0 \\
0 & 0 & 2t^2\Delta & 0 & \sqrt{2}t^2\xi & 0 & 2t^2\Delta & 0 & 0 \\
0 & 0 & 0 & 0 & 0 & \frac{-2t^2}{g_2} & 0 & \frac{-2t^2}{g_2} & 0 \\
0 & 0 & 0 & 0 & 0 & 0 & 0 & 0 & \frac{-4t^2}{g_2}
\end{pmatrix} \tag{A.10}
$$

A.2 | Bilinear Biquadratic Heisenberg Hamiltonian

In the previous section, we found the matrix representation of the Bose Hubbard Hamiltonian for spin 1 particles, now this effective Hamiltonian can be mapped in terms of spin 1 matrices. We can start by considering a general decomposition:

$$
\hat{H} = Q\sum_i (\hat{S}_i^z)^2 + a_1(\hat{S}_1 \cdot \hat{S}_2) + a_2(\hat{S}_1 \cdot \hat{S}_2)^2 + a_3(\hat{S}_1^x \cdot \hat{S}_2^x + \hat{S}_1^y \cdot \hat{S}_2^y)^2 + a_4(\hat{S}_1^z \cdot \hat{S}_2^z)^2 \tag{A.11}
$$

Considering that,

$$
\hat{S}_i^x = \frac{\hat{S}_i^+ + \hat{S}_i^-}{2}, \qquad \hat{S}_i^y = \frac{\hat{S}_i^+ - \hat{S}_i^-}{2i} = \frac{-i}{2}(\hat{S}_i^+ - \hat{S}_i^-).
$$

Performing the matrix operation:

$$
\hat{\vec{S}}_1 \cdot \hat{\vec{S}}_2 = \hat{S}_1^x \cdot \hat{S}_2^x + \hat{S}_1^y \cdot \hat{S}_2^y + \hat{S}_1^z \cdot \hat{S}_2^z.
$$

$$\hat{H} = \begin{pmatrix} a_1+a_2+a_4+2Q & 0 & 0 & 0 & 0 & 0 & 0 & 0 & 0 \\ 0 & a_2+a_3+Q & 0 & a_1 & 0 & 0 & 0 & 0 & 0 \\ 0 & 0 & -a_1+2a_2+a_3+a_4+2Q & 0 & a_1-a_2 & 0 & a_2+a_3 & 0 & 0 \\ 0 & a_1 & 0 & a_2+a_3+Q & 0 & 0 & 0 & 0 & 0 \\ 0 & 0 & a_1-a_2 & 0 & 2a_2+2a_3 & 0 & a_1-a_2 & 0 & 0 \\ 0 & 0 & 0 & 0 & 0 & a_2+a_3+Q & 0 & a_1 & 0 \\ 0 & 0 & a_2+a_3 & 0 & a_1-a_2 & 0 & -a_1+2a_2+a_3+a_4+2Q & 0 & 0 \\ 0 & 0 & 0 & 0 & 0 & a_1 & 0 & a_2+a_3+Q & 0 \\ 0 & 0 & 0 & 0 & 0 & 0 & 0 & 0 & a_1+a_2+a_4+2Q \end{pmatrix}$$

Such that the matrix representation of the decomposition A.11 is given by:

By comparing this matrix with A.10, we can establish a relationship between the constants,

$$a_1 = \frac{-2t^2}{g_2} \qquad a_2 = \frac{4t^2}{3g_0} - \frac{-2t^2}{3g_2} \qquad a_3 = a_4 = \mathcal{O}(t^4) \approx 0$$

Defining a_1 and a_2 as $a_1 = -Jcos\theta$ and $a_2 = -Jsin\theta$, we express the relevant parameters of the system:

$$tan\theta = \frac{a_2}{a_1} = \frac{2g_2+g_0}{3g_0} \tag{A.12}$$

$$J = \sqrt{a_1^2+a_2^2} = \frac{2t^2}{3g_0g_2}\sqrt{10g_0^2+4g_0g_2+4g_2^2} \tag{A.13}$$

Where we take the hopping parameter $J = 1$ and the angle $\theta \in [-\pi/2, -\pi + tan^{-1}(1/3)]$ and $D = -Q/J$. Hence, the effective Hamiltonian matches with the Heisenberg bilinear biquadratic Hamiltonian,

$$\hat{H} = -J\sum_i \Big(cos(\theta)\hat{S}_i \cdot \hat{S}_{i+1} + sin(\theta)\Big(\hat{S}_i \cdot \hat{S}_{i+1}\Big)^2 + D(\hat{S}_i^z)^2 \Big). \tag{A.14}$$

B Coupled Differential Equations

This section is devoted to the derivation of the coupled differential equations with which the dynamics of the system is studied. Initially the equations were calculated for the spinless Bose-Hubbard model and later for the biquadratic bilinear Heisenberg model.

B.1 | One-site Gutzwiller for spinless Bose-Hubbard Model

$$\hat{H}_{BH} = -t \sum_{\langle ij \rangle} \left(\hat{a}_i^+ \hat{a}_j + \hat{a}_j^+ \hat{a}_i \right) + \frac{u}{2} \sum_i \hat{n}_i \left(\hat{n}_i - \hat{\mathbb{1}} \right) - \mu \sum_i \hat{n}_i \tag{B.1}$$

Before obtaining the Euler-Lagrange equations, it is necessary to calculate the Lagrangian in (put number of the equation). Such that the state and its derivative are given by:

$$\boxed{|\psi\rangle = \otimes_i \sum_{n_i=0} f_{n_i}^i |n_i\rangle \quad ; \quad \langle\psi| = \otimes_k \sum_{n_k=0}^{k} f_{n_k} \langle n_k|} \tag{B.2}$$

$$|\dot{\psi}\rangle = \sum_j \left(\otimes_i^{j-1} \sum_{n_i} f_{n_i}^i |n_i\rangle \right) \left(\sum_{n_j} \dot{f}_{n_j}^j |n_j\rangle \right) \left(\sum_{j+1}^{L} \sum_{n_{j+1}} f_{n_{j+1}}^{j+1} |n_{j+1}\rangle \right) \tag{B.3}$$

$$\langle\dot{\psi}| = \sum_{j'} \left(\otimes_k^{j'-1} \sum_{n_k} f_{n_k}^{*k} \langle n_k| \right) \left(\sum_{n_j} \dot{f}_{n_j}^{j'} \langle n_j| \right) \left(\sum_{j'+1}^{L} \sum_{n_{j-1}} f_{n_{j+1}}^{*j+1} \langle n_{j'+1}| \right) \tag{B.4}$$

Then, the inner product is given by

$$\begin{aligned}\langle\psi\,|\,\dot{\psi}\rangle &= \sum_j \left(\otimes_k \sum_{n_k} f^{*k}_{n_k}\langle n_k|\right)\left[\left(\otimes_i^{j-1}\sum_{n_i} f^{i}_{n_i}|n_i\rangle\right)\left(\sum_{n_j}\dot{f}^{j}_{n_j}|n_j\rangle\right)\left(\otimes_{j+1}^{L}\sum_{n_{j+1}}|n_{j+1}\rangle\right)\right] \\ &= \sum_j \left(\otimes_k^{j-1}\sum_{n_k,n_i} f^{*k}_{n_k} f^{i}_{n_i}\underbrace{\langle n_k|n_i\rangle}\right)\left(\sum_{n_k,n_j} f^{*k}_{n_k}\dot{f}^{j}_{n_j}\underbrace{\langle n_k|n_j\rangle}\right)\left(\otimes_{j+1}^{L}\sum_{n_{j+1},n_k} f^{*k}_{n_k} f^{j+1}_{n_{j+1}}\underbrace{\langle n_k|n_{j+1}\rangle}\right) \\ &= \sum_j \left(\otimes_i^{j-1}\sum_{n_i} f^{*i}_{n_i} f^{i}_{n_i}\right)\left(\sum_{n_j} f^{*j}_{n_j}\dot{f}^{j}_{n_j}\right)\left(\otimes_{j+1}^{L}\sum_{n_{j+1}} f^{*j+1}_{n_{j+1}} f^{j+1}_{n_{j+1}}\right)\end{aligned} \tag{B.5}$$

$$\boxed{\langle\psi|\dot{\psi}\rangle = \sum_j \left(\otimes_i^{j-1}\sum_{n_i}|f^{i}_{n_i}|^2\right)\left(\sum_{n_j} f^{*j}_{n_j}\dot{f}^{j}_{n_j}\right)\left(\otimes_{j+1}^{L}\sum_{n_{j+1}}|f^{j+1}_{n_{j+1}}|^2\right)} \tag{B.6}$$

By doing an analogous process, the conjugate of the previous product can be obtained,

$$\boxed{\langle\dot{\psi}|\psi\rangle = \sum_j \left(\otimes_i^{j-1}\sum_{n_i}|f^{i}_{n_i}|^2\right)\left(\sum_{n_j} \dot{f}^{*j}_{n_j} f^{j}_{n_j}\right)\left(\otimes_{j+1}^{L}\sum_{n_{j+1}}|f^{j+1}_{n_{j+1}}|^2\right)} \tag{B.7}$$

Then, due to normalization,

$$\begin{aligned}&\sum_{n_i}|f^{i}_{n_i}|^2 = 1 \\ &\rightarrow \langle\psi|\dot{\psi}\rangle = \sum_j\sum_{n_j} f^{*j}_{n_j}\dot{f}^{j}_{n_j} \\ &\rightarrow \langle\dot{\psi}|\psi\rangle = \sum_j\sum_{n_j} \dot{f}^{*j}_{n_j} f^{j}_{n_j}\end{aligned} \tag{B.8}$$

So that the first part of the Lagrangian,

$$\boxed{\mathcal{L}_1 = \sum_j\sum_{n_j}\left(f^{*j}_{n_j}\dot{f}^{j}_{n_j} - \dot{f}^{*j}_{n_j} f^{j}_{n_j}\right)} \tag{B.9}$$

Now for $\mathcal{L}_2$, it's necessary to calculate the expectation values for the three terms of the Hamiltonian:

$$\mathcal{L}_2 = \langle\psi|\hat{H}|\psi\rangle$$

We calculate the expected values of the three terms of the Hamiltonian separately,

- Hopping term

$$
\begin{aligned}
&-t\langle\psi|\sum_{\langle i,j\rangle}\hat{a}_i^\dagger\hat{a}_j+\hat{a}_j^\dagger\hat{a}_i|\psi\rangle\\
&\rightarrow\langle\psi|\hat{a}_i^\dagger\underbrace{\hat{a}_j|\psi\rangle}\\
&\qquad\hat{a}_j|\psi\rangle=\cdots\otimes\sum_{n_i}f_{n_i}^i|n_i\rangle\otimes\sum_{n_j}f_{n_j}^j\sqrt{n_j}|n_j-1\rangle\otimes\cdots\\
&\qquad\qquad\hookrightarrow\text{the rest of the terms remains unchangeable}\hookleftarrow
\end{aligned}
\tag{B.10}
$$

$$
\boxed{\langle\psi|\hat{a}_i^\dagger\hat{a}_j|\psi\rangle=\sum_i\left(\sum_{n_i}f_{n_i'}^{*i'}f_{n_i}^i\sqrt{n_i+1}\otimes\sum_{n_{i+1}}f_{n_{i+1}-1}^{*(i+1)}f_{n_{i+1}}^{(i+1)}\sqrt{n_{i+1}}\right)}
\tag{B.11}
$$

$$
\begin{aligned}
&\rightarrow\langle\psi|\hat{a}_j^\dagger\underbrace{\hat{a}_i|\psi\rangle}\\
&\qquad\hat{a}_i|\psi\rangle=\cdots\otimes\sum_{n_i}f_{n_i}^i\sqrt{n_i}|n_i-1\rangle\otimes\sum_{n_j}f_{n_j}^j|n_j\rangle\otimes\cdots\\
&\qquad\qquad\hookrightarrow\text{the rest of the terms remains unchangeable}\hookleftarrow
\end{aligned}
\tag{B.12}
$$

$$
\boxed{\langle\psi|\hat{a}_j^\dagger\hat{a}_i|\psi\rangle=\sum_i\left(\sum_{n_i}f_{n_i}^{*i}f_{n_i}^i\sqrt{n_i}\otimes\sum_{n_{i+1}}f_{n_{i+1}+1}^{*(i+1)}f_{n_{i+1}}^{(i+1)}\sqrt{n_{i+1}+1}\right)}
\tag{B.13}
$$

- Interaction term

$$
\begin{aligned}
\langle\psi|\frac{U}{2}\sum_i\hat{n}_i(\hat{n}_i-\mathbb{1})|\psi\rangle&=\frac{U}{2}\langle\psi|\sum_i\sum_{n_i=0}f_{n_i}^i\cdot n_i(n_i-1)|n_i\rangle\\
&=\frac{U}{2}\left(\otimes_k\sum_{n_k=0}f_{n_k}^{*k}\langle n_k|\right)\left(\sum_i\sum_{n_i=0}f_{n_i}^i\cdot n_i(n_i-1)|n_i\rangle\right)
\end{aligned}
\tag{B.14}
$$

$$
\boxed{\langle\psi|\hat{H}_{int}|\psi\rangle=\frac{U}{2}\sum_i\left[\sum_{n_i=0}|f_{n_i}^i|^2\cdot n_i(n_i-1)\right]}
\tag{B.15}
$$

- Chemical potential term

$$\langle\psi|-\mu\sum_i \hat{n}_i|\psi\rangle = -\mu\langle\psi|\sum_i\sum_{n_i} f^i_{n_i}\hat{n}_i|n_i\rangle \tag{B.16}$$
$$= -\mu\sum_i\left(\otimes_k\sum_{n_k=0} f^{*k}_{n_k}\langle n_k|\right)\left(\sum_{n_i=0} f^i_{n_i}\cdot n_i|n_i\rangle\right)$$

$$\boxed{\langle\psi|\hat{H}_\mu|\psi\rangle = -\mu\sum_i\sum_{n_i=0}|f^i_{n_i}|^2 n_i} \tag{B.17}$$

Collecting all those terms together we obtain the second part of the Lagrangian. Now corresponds to compute the derivatives to obtain the Euler-Lagrange equations:

- $$\frac{d}{dt}\left(\frac{\partial\mathcal{L}_1}{\partial\dot{f}^{*i}_{n_i}}\right) = \frac{\partial\mathcal{L}_1}{\partial f^{*i}_{n_i}} \tag{B.18}$$

- $$\frac{d}{dt}\left(\frac{\partial\mathcal{L}_2}{\partial\dot{f}^{*i}_{n_i}}\right) = \frac{\partial\mathcal{L}_2}{\partial f^{*i}_{n_i}} \tag{B.19}$$

For the first part of the Lagrangian $\mathcal{L}_1$,
$\rightarrow$ RHS:

$$\frac{\partial\mathcal{L}_1}{\partial\dot{f}^{*i}_{n_i}} = \frac{i\hbar}{2}\sum_j\sum_{n_j}\frac{\partial}{\partial\dot{f}^{*i}_{n_i}}\left(f^{*j}_{n_j}\dot{f}^j_{n_j} - (\dot{f}^{*j}_{n_j}(f^j_{n_j}\right) \tag{B.20}$$
$$= -\frac{i\hbar}{2}f^j_{n_j}\delta_{n_i n_j}\delta_{ij}$$
$$= -\frac{i\hbar}{2}f^i_{n_i}$$

$\rightarrow$ LHS:

$$\frac{\partial\mathcal{L}_1}{\partial f^{*i}_{n_i}} = \frac{i\hbar}{2}\sum_j\sum_{n_j}\frac{\partial}{\partial f^{*i}_{n_i}}\left(f^{*j}_{n_j}\dot{f}^j_{n_j} - (\dot{f}^{*j}_{n_j}(f^j_{n_j}\right) \tag{B.21}$$
$$= -\frac{i\hbar}{2}f^j_{n_j}\delta_{n_i n_j}\delta_{ij}$$
$$= -\frac{i\hbar}{2}f^i_{n_i}$$

Thus, the differential equation:

$$\boxed{-i\hbar\frac{d}{dt}f^i_{n_i}=0} \tag{B.22}$$

For the second part of the Lagrangian $\mathcal{L}_2$,

Since $\mathcal{L}_2$ does not depend on $\dot{f}^{*i}_{n_i}$,

$$\begin{aligned}\frac{\partial\mathcal{L}_2}{\partial\dot{f}^{*i}_{n_i}}&=0\\ \frac{d}{dt}\left(\frac{\partial\mathcal{L}_2}{\partial\dot{f}^{*i}_{n_i}}\right)&=0\end{aligned} \tag{B.23}$$

Now let's calculate the derivatives for the three terms in $\mathcal{L}_2$

- Hopping term in (B.11 & B.13)

$$\frac{\partial}{\partial f^{*k}_{n'_k}}\sum_i\left[\sum_{n_i}f^{*i}_{n_i+1}f^i_{n_i}\sqrt{n_i+1}\otimes\sum_{n_{i+1}}f^{*(i+1)}_{n_{i+1}-1}f^{(i+1)}_{n_{i+1}}\sqrt{n_{i+1}}+\sum_{n_i}f^{*i}_{n_i-1}f^i_{n_i}\sqrt{n_i}\otimes\sum_{n_{i+1}}f^{*(i+1)}_{n_{i+1}+1}f^{(i+1)}_{n_{i+1}}\sqrt{n_{i+1}+1}\right] \tag{B.24}$$

Splitting by two the expression,

$$\begin{aligned}\rightarrow&\frac{\partial}{\partial f^{*k}_{n'_k}}\sum_i\Big[\sum_{n_i}f^{*i}_{n_i+1}f^i_{n_i}\sqrt{n_i+1}\otimes\sum_{n_{i+1}}f^{*(i+1)}_{n_{i+1}-1}f^{(i+1)}_{n_{i+1}}\sqrt{n_{i+1}}\Big]\\&=\Big(f^i_{n_i}\sqrt{n_i+1}\delta_{ik}\delta_{n'_k,n_{i+1}}\Big)\otimes\sum_{n_{i+1}}f^{*(i+1)}_{n_{i+1}-1}f^{(i+1)}_{n_{i+1}}{}_{i+1}\\&+\sum_{n_i}f^{*i}_{n_i+1}f^i_{n_i}\sqrt{n_i+1}\otimes\Big(f^{(i+1)}_{n_{i+1}}\sqrt{n_{i+1}}\delta_{i+1,k}\delta_{n'_k,n_{i+1}-1}\Big)\\&=f^k_{n'_{k-1}}\sqrt{n'_k}\otimes\sum_{n_{i+1}}f^{*(k+1)}_{n_{k+1}-1}f^{(k+1)}_{n_{k+1}}\sqrt{n_{k+1}}+\sum_{n_{k-1}}f^{*(k-1)}_{n_{k-1}+1}f^{(k-1)}_{n_{k-1}}\sqrt{n_{k-1}+1}\otimes f^k_{n'_k+1}\sqrt{n'_k+1}\end{aligned}$$

$$\rightarrow\frac{\partial}{\partial f^{*i}_{n_i-1}}\sum_i\left[\sum_{n_i}f^{*i}_{n_i-1}f^i_{n_i}\sqrt{n_i}\otimes\sum_{n_{i+1}}\right]$$

B.2 | One-site Gutzwiller for Heisenberg Model

Para este caso consideraremos el Hamiltoniano de Heisenberg biquadrático bilineal descrito en el apéndice A (ref).

For the spin-1 case it's necessary to modify the Gutzwiller ansatz since we're now interested in the magnetic projections,

$$|\psi\rangle = \prod_i \sum_{m_i=-1}^{1} f^i_{m_i} |m_i\rangle \tag{B.25}$$

In order to calculate the expectation values, let's decompose the Hamiltonian in three parts:

$$\hat{H} = -J \sum_{\langle i,j \rangle} \left[cos\theta \hat{S}^{(i)} \hat{S}^{(j)} + sin\theta \left(\hat{S}^{(i)} \cdot \hat{S}^{(j)} \right)^2 \right] - JD \sum_i \left(\hat{S}^{(i)}_z \right)^2 \tag{B.26}$$

- Let's consider the orange part of the Hamiltonian above,

$$\begin{aligned} \hat{H} &= -J \sum_{\langle i,j \rangle} cos\theta \left(\hat{S}^i_z \hat{S}^j_z + \hat{S}^i_x \hat{S}^j_x + \hat{S}^i_y \hat{S}^j_y \right) \\ &= -J \sum_{\langle i,j \rangle} cos\theta \left[\hat{S}^i_z \hat{S}^j_z + \frac{1}{2} \left(\hat{S}^i_+ \hat{S}^j_- + \hat{S}^i_- \hat{S}^j_+ \right) \right] \end{aligned}$$

The expectation value is given by

$$\rightarrow \langle \psi | \hat{S}^i_z \hat{S}^j_z | \psi \rangle = \sum_{m_i} |f^i_{m_i}|^2 \cdot m_i \otimes \sum_{m_j} |f^j_{m_j}|^2 \cdot m_j \tag{B.27}$$

$$\begin{aligned} \rightarrow \frac{1}{2} \langle \psi | \left(\hat{S}^i_+ \hat{S}^j_- + \hat{S}^i_- \hat{S}^j_+ \right) | \psi \rangle = & \frac{1}{2} \left[\sum_i f^i_{m_i} f^*_{m_i+1} i \sqrt{2 - m_i(m_i+1)} \otimes \sum_j f^j_{m_j} f^*_{m_j-1} j \sqrt{2 - m_j(m_j-1)} \right] \\ & + \sum_i f^i_{m_i} f^*_{m_i-1} i \sqrt{2 - m_i(m_i-1)} \otimes \sum_j f^j_{m_j} f^*_{m_j+1} j \sqrt{2 - m_j(m_j+1)} \end{aligned}$$

- Let's consider the cyan part of the Hamiltonian above,

$$\hat{H} = DJ \sum_i \left(\hat{S}^i_z \right)^2 \tag{B.28}$$

The expectation value,

$$\rightarrow \langle \psi | \hat{H} | \psi \rangle = DJ \sum_i |f^i_{m_i}|^2 \cdot m_i^2 \tag{B.29}$$

- Let's consider the green part of the Hamiltonian above,

$$\begin{aligned}\hat{H} &= -J\sum_{\langle i,j\rangle} sin\theta\left[\hat{S}_z^i\hat{S}_z^j + \frac{1}{2}\left(\hat{S}_+^i\hat{S}_-^j + \hat{S}_-^i\hat{S}_+^j\right)\right]^2 \\ &= -J\sum_{\langle i,j\rangle} sin\theta\Big[\hat{S}_z^i\hat{S}_z^j\cdot\hat{S}_z^i\hat{S}_z^j + \frac{1}{2}\hat{S}_z^i\hat{S}_z^j\cdot\hat{S}_+^i\hat{S}_-^j + \frac{1}{2}\hat{S}_z^i\hat{S}_z^j\cdot\hat{S}_-^i\hat{S}_+^j + \frac{1}{2}\hat{S}_-^i\hat{S}_+^j\cdot\hat{S}_z^i\hat{S}_z^j + \frac{1}{2}\hat{S}_+^i\hat{S}_-^j\cdot\hat{S}_z^i\hat{S}_z^j \\ &+ \frac{1}{2}\hat{S}_+^i\hat{S}_-^j\cdot\hat{S}_-^i\hat{S}_+^j + \frac{1}{4}\hat{S}_+^i\hat{S}_-^j\cdot\hat{S}_+^i\hat{S}_-^j + \frac{1}{4}\hat{S}_-^i\hat{S}_+^j\cdot\hat{S}_+^i\hat{S}_-^j + \frac{1}{4}\hat{S}_-^i\hat{S}_+^j\cdot\hat{S}_-^i\hat{S}_+^j\Big].\end{aligned}$$

The calculation of the expected value is analogous to what was done for the cyan and orange part above. Collecting all the terms, the expected value of the Hamiltonian looks like:

$$\begin{aligned}\langle\hat{H}\rangle = -\mathrm{J}\sum_{\langle ij\rangle} cos\theta\Big[&\sum_i |f_{m_i}^i|^2 m_i \otimes \sum_j |f_{m_j}^j|^2 m_j + \frac{1}{2}\Big(\sum_i f_{m_i}^i f_{m_i+1}^{*i}\sqrt{2-m_i(m_i+1)}\otimes\sum_j f_{m_j}^j f_{m_j-1}^{*j} \\ &\sqrt{2-m_j(m_j-1)} + \sum_i f_{m_i}^i f_{m_i-1}^{*i}\sqrt{2-m_i(m_i-1)}\otimes\sum_j f_{m_j}^j f_{m_j+1}^{*j}\sqrt{2-m_j(m_j+1)}\Big)\Big] \\ -J\sum_{\langle ij\rangle} sin\theta\Big[&\sum_i |f_{m_i}^i|^2 m_i^2 \otimes \sum_j |f_{m_j}^j|^2 m_j^2 + \frac{1}{2}\sum_i f_{m_i}^i f_{m_i+1}^{*i}(m_i+1)\sqrt{2-m_i(m_i+1)} \\ &\otimes\sum_j f_{m_j}^j f_{m_j-1}^{*j}(m_j-1)\sqrt{2-m_j(m_j-1)} + \frac{1}{2}\sum_i f_{m_i}^i f_{m_i-1}^{*i}(m_i-1)\sqrt{2-m_i(m_i-1)} \\ &\otimes\sum_j f_{m_j}^j f_{m_j+1}^{*j}(m_j+1)\sqrt{2-m_j(m_j+1)} + \frac{1}{2}\sum_i f_{m_i}^i f_{m_i+1}^{*i} m_i\sqrt{2-m_i(m_i+1)}\otimes\sum_j f_{m_j}^j f_{m_j-1}^{*j} m_j \\ &\sqrt{2-m_j(m_j-1)} + \frac{1}{2}\sum_i f_{m_i}^i f_{m_i-1}^{*i} m_i\sqrt{2-m_i(m_i-1)}\otimes\sum_j f_{m_j}^j f_{m_j+1}^{*j} m_j\sqrt{2-m_j(m_j+1)} \\ &+ \frac{1}{4}\sum_i f_{m_i}^i f_{m_i+2}^{*i}\sqrt{2-m_i(m_i+1)}\sqrt{2-(m_i+1)(m_i+2)}\otimes\sum_j f_{m_j}^j f_{m_j-2}^{*j}\sqrt{2-m_j(m_j-1)} \\ &\sqrt{2-(m_j-1)(m_j-2)} + \frac{1}{4}\sum_i f_{m_i}^i f_{m_i}^{*i}\sqrt{2-m_i(m_i-1)}\sqrt{2-m_i(m_i-1)}\otimes\sum_j f_{m_j}^j f_{m_j}^{*j} \\ &\sqrt{2-m_j(m_j+1)}\sqrt{2-m_j(m_j+1)} + \frac{1}{4}\sum_i f_{m_i}^i f_{m_i}^{*i}\sqrt{2-m_i(m_i+1)}\sqrt{2-m_i(m_i+1)} \\ &\otimes\sum_j f_{m_j}^j f_{m_j}^{*j}\sqrt{2-m_j(m_j-1)}\sqrt{2-m_j(m_j-1)} + \frac{1}{4}\sum_i f_{m_i}^i f_{m_i-2}^{*i}\sqrt{2-m_i(m_i-1)} \\ &\sqrt{2-(m_i-1)(m_i-2)}\otimes\sum_j f_{m_j}^j f_{m_j+2}^{*j}\sqrt{2-m_j(m_j+1)}\sqrt{2-(m_j+1)(m_j+2)} + \mathrm{DJ}\sum_i |f_{m_i}^i|^2 m_i^2.\end{aligned}$$

Once we have obtained the Lagrangian of the system,

$$\mathcal{L} = \frac{i\hbar}{2}(\langle\psi|\dot{\psi}\rangle - \langle\dot{\psi}|\psi\rangle) - \langle\psi|\hat{H}|\psi\rangle, \tag{B.30}$$

we can perform the derivatives,

$$\begin{aligned}
i\hbar\frac{d}{dt}f^k_{m'_k} = &-\mathrm{J}\sum_{\langle ij\rangle}\sum_m \cos\theta\Big[\sum_i\Big(f^i_n|f^{i+1}_m|^2 m\cdot n + f^i_n|f^{i-1}_m|^2 m\cdot n\Big)\\
&+\Big(\frac{1}{2}f^i_{n-1}\Omega(n)\cdot f^{i+1}_m f^{*i+1}_{m-1}\Omega(m) + \frac{1}{2}f^i_n\Omega(n+1)\cdot f^{i-1}_m f^{*i-1}_{m+1}\Omega(m+1)\Big)\\
&+(\frac{1}{2}f^i_{n+1}\Omega(n+1)\cdot f^{i+1}_m f^{*i+1}_{m+1}\Omega(m+1) + \frac{1}{2}f^i_n\Omega(n+1)\cdot f^{i+1}_m f^{*i+1}_{m-1}\Omega(m))\Big]\\
&-\mathrm{J}\sum_{\langle ij\rangle}\sum_m \sin\theta\Big[f^i_n|f^{i+1}_m|^2 m^2\cdot n^2 + f^i_n|f^{i-1}_m|^2 m^2\cdot n^2 + \frac{1}{2}\Big(f^i_{n-1}n\Omega(n)\cdot f^{i+1}_m f^{*i+1}_{m-1}(m-1)\Omega(m)\\
&+f^i_{n+1}n\Omega(n+1)\cdot f^{i-1}_m f^{*i-1}_{m+1}(m+1)\Omega(m+1)\Big) + \frac{1}{2}\Big(f^i_{n+1}n\Omega(n+1)\cdot f^{i+1}_m f^{*i+1}_{m+1}(m+1)\Omega(m+1)\\
&+f^i_{n-1}n\Omega(n)\cdot f^{i-1}_m f^{*i-1}_{m-1}(m-1)\Omega(m)\Big) + \frac{1}{2}\Big(f^i_{n-1}(n-1)\Omega(n)\cdot f^{i+1}_m f^{*i+1}_{m-1}m\Omega(m)\\
&+f^i_{n+1}(n+1)\Omega(n+1)\cdot f^{i-1}_m f^{*i-1}_{m+1}m\Omega(m+1)\Big) + \frac{1}{2}\Big(f^i_{n+1}(n+1)\Omega(n+1)\cdot f^{i+1}_m f^{*i+1}_{m+1}m\Omega(m+1)\\
&+f^i_{n-1}(n-1)\Omega(n)\cdot f^{i-1}_m f^{*i-1}_{m-1}m\Omega(m)\Big) + \frac{1}{4}\Big(f^i_{n-2}\Omega(n-1)\Omega(n)\cdot f^{i+1}_m f^{*i+1}_{m-2}\Omega(m)\Omega(m-1)\\
&+f^{i-1}_m f^{*i-1}_{m+2}\Omega(m+1)\Omega(m+2)\cdot f^i_{n+2}\Omega(n+2)\Omega(n+1)\Big) + \frac{1}{4}\Big(f^i_n\Omega(n)^2\cdot f^{i+1}_m f^{*i+1}_m\Omega(m+1)^2\\
&+f^i_n\Omega(n+1)^2\cdot f^{i-1}_m f^{*i-1}_m\Omega(m)^2\Big) + \frac{1}{4}\Big(f^i_n\Omega(n+1)^2\cdot f^{i+1}_m f^{*i+1}_m\Omega(m)^2\\
&+f^i_n\Omega(n)^2\cdot f^{i-1}_m f^{*i-1}_m\Omega(m+1)^2\Big) + \frac{1}{4}\Big(f^i_{n+2}\Omega(n+2)\Omega(n+1)\cdot f^{i+1}_m f^{*i+1}_{m+2}\Omega(m+1)\Omega(m+2)\\
&+f^{i-1}_m f^{*i-1}_{m-2}\Omega(m-1)\Omega(m)\cdot f^i_{n-2}\Omega(n-1)\Omega(n)\Big] + \mathrm{DJ}\sum_n f^i_n n^2.
\end{aligned}$$

B.3 | Two-site Gutzwiller for Heisenberg model

The derivation of the equations for two sites is analogous to the previous section, except that this time the state will be in the form:

$$|\psi\rangle = \prod_i \sum_{m_a,m_b} f^i_{m_a,m_b}|m_a,m_b\rangle \tag{B.31}$$

In order to calculate the expectation values of the Hamiltonian, we need to take into account that the operators for the two-site expansion look obey:

- $\hat{S}_z^i \cdot \hat{S}_z^j \rightarrow (\hat{S}_z^{i_a} + \hat{S}_z^{i_a})(\hat{S}_z^{j_b} + \hat{S}_z^{j_b})$
- $\hat{S}_+^i \cdot \hat{S}_-^j \rightarrow (\hat{S}_+^{i_a} + \hat{S}_+^{i_b})(\hat{S}_-^{j_a} + \hat{S}_-^{j_b})$

In addition to the above consideration, the derivation of the Lagrangian and the subsequent derivation of the equations follows the same process as indicated in the derivation of the differential equations for the Gutzwiller for one site.

$$
\begin{aligned}
i\hbar\frac{d}{dt}(f^{k_a k_b}_{m_{k_a} m_{k_b}}) = -\mathrm{J}\sum_{\langle ij\rangle}\cos\theta\Big[&\sum_{m_a m_b} f^i_{n_a n_b}|f^{i+1}_{m_a m_b}|^2(n_a+n_b)(m_a+m_b) + f^i_{n_a n_b}|f^{i-1}_{m_a m_b}|^2(n_a+n_b)(m_a+m_b)\\
&+\frac{1}{2}\sum_{m_a m_b}\Big(f^i_{n_a-1 n_b}\sqrt{2-(n_a-1)n_a} + f^i_{n_a n_b-1}\sqrt{2-(n_b-1)n_b}\Big)\Big(f^{i+1}_{m_a m_b} f^{*i+1}_{m_a-1 m_b}\sqrt{2-m_a(m_a-1)}\\
&+f^{i+1}_{m_a m_b} f^{*i+1}_{m_a m_b-1}\sqrt{2-m_b(m_b-1)}\Big) + \Big(f^{i-1}_{m_a m_b} f^{*i-1}_{m_a+1 m_b}\sqrt{2-m_a(m_a+1)} + f^{i-1}_{m_a m_b} f^{*i-1}_{m_a m_b+1}\sqrt{2-m_b(m_b+1)}\Big)\\
&\Big(f^i_{n_a n_b}\sqrt{2-(n_a+1)n_a} + f^i_{n_a n_b}\sqrt{2-(n_b+1)n_b}\Big) + \frac{1}{2}\sum_{m_a m_b}\Big(f^i_{n_a+1 n_b}\sqrt{2-(n_a+1)n_a} + f^i_{n_a n_b+1}\sqrt{2-(n_b+1)n_b}\Big)\\
&\Big(f^{i+1}_{m_a m_b} f^{*i+1}_{m_a+1 m_b}\sqrt{2-m_a(m_a+1)} + f^{i+1}_{m_a m_b} f^{*i+1}_{m_a m_b+1}\sqrt{2-m_b(m_b+1)}\Big) + \Big(f^{i-1}_{m_a m_b} f^{*i-1}_{m_a-1 m_b}\sqrt{2-m_a(m_a-1)}\\
&+f^{i-1}_{m_a m_b} f^{*i-1}_{m_a m_b-1}\sqrt{2-m_b(m_b-1)}\Big)\Big(f^i_{n_a n_b}\sqrt{2-(n_a-1)n_a} + f^i_{n_a n_b}\sqrt{2-(n_b-1)n_b}\Big)\Big]\\
+\sum_{\langle ij\rangle}\sin\theta\Big[&\Big[2f^i_{n_a n_b}|f^i_{n_a n_b}|^2(n_a+n_b)^2\cdot|f^{i+1}_{n_a n_b}|^4(m_a+m_b)^2 + 2f^i_{n_a n_b}|f^i_{n_a n_b}|^2(n_a+n_b)^2\cdot|f^{i-1}_{n_a n_b}|^4(m_a+m_b)^2\Big]\\
&+\frac{1}{2}\Big[(f^i_{n_a-1 n_b} n_a\sqrt{2-(n_a-1)n_a} + f^i_{n_a n_b-1} n_b\sqrt{2-(n_b-1)n_b})(f^{*i+1}_{m_a-1 m_b} f^{i+1}_{m_a m_b}(m_a-1)\sqrt{2-(m_a-1)m_a}\\
&+f^{*i+1}_{m_a m_b-1} f^{i+1}_{m_a m_b}(m_b-1)\sqrt{2-(m_b-1)m_b}) + (f^{*i-1}_{m_a+1 m_b} f^{i-1}_{m_a m_b}(m_a+1)\sqrt{2-(m_a+1)m_a}\\
&+f^{*i-1}_{m_a m_b+1} f^{i-1}_{m_a m_b}(m_b+1)\sqrt{2-(m_b+1)m_b})(f^i_{n_a+1 n_b} n_a\sqrt{2-(n_a+1)n_a} + f^i_{n_a n_b+1} n_b\sqrt{2-(n_b+1)n_b})\Big]\\
&+\frac{1}{2}\Big[(f^i_{n_a+1 n_b} n_a\sqrt{2-(n_a+1)n_a} + f^i_{n_a n_b+1} n_b\sqrt{2-(n_b+1)n_b})(f^{*i+1}_{m_a+1 m_b} f^{i+1}_{m_a m_b}(m_a+1)\sqrt{2-(m_a+1)m_a}\\
&+f^{*i+1}_{m_a m_b+1} f^{i+1}_{m_a m_b}(m_b+1)\sqrt{2-(m_b+1)m_b}) + (f^{*i-1}_{m_a-1 m_b} f^{i-1}_{m_a m_b}(m_a-1)\sqrt{2-(m_a-1)m_a}\\
&+f^{*i-1}_{m_a m_b-1} f^{i-1}_{m_a m_b}(m_b-1)\sqrt{2-(m_b-1)m_b})(f^i_{n_a-1 n_b} n_a\sqrt{2-(n_a-1)n_a} + f^i_{n_a n_b-1} n_b\sqrt{2-(n_b-1)n_b})\Big]\\
&+\frac{1}{2}\Big[(f^i_{n_a-1 n_b}(n_a-1)\sqrt{2-(n_a-1)n_a} + f^i_{n_a n_b-1}(n_b-1)\sqrt{2-(n_b-1)n_b})(f^{*i+1}_{m_a-1 m_b} f^{i+1}_{m_a m_b}(m_a)\sqrt{2-(m_a-1)m_a}\\
&+f^{*i+1}_{m_a m_b-1} f^{i+1}_{m_a m_b}(m_b-1)\sqrt{2-(m_b-1)m_b}) + (f^{*i-1}_{m_a+1 m_b} f^{i-1}_{m_a m_b}(m_a)\sqrt{2-(m_a+1)m_a}\\
&+f^{*i-1}_{m_a m_b+1} f^{i-1}_{m_a m_b}(m_b)\sqrt{2-(m_b+1)m_b})(f^i_{n_a+1 n_b}(n_a+1)\sqrt{2-(n_a+1)n_a} + f^i_{n_a n_b+1}(n_b+1)\sqrt{2-(n_b+1)n_b})\Big]
\end{aligned}
$$

$$+\frac{1}{2}\Big[(f^{i}_{n_a+1n_b}(n_a+1)\sqrt{2-(n_a+1)n_a}+f^{i}_{n_an_b+1}(n_b+1)\sqrt{2-(n_b+1)n_b})(f^{*i+1}_{m_a+1m_b}f^{i+1}_{m_am_b}(m_a)\sqrt{2-(m_a+1)m_a}$$
$$+f^{*i+1}_{m_am_b+1}f^{i+1}_{m_am_b}(m_b)\sqrt{2-(m_b+1)m_b})+(f^{*i-1}_{m_a-1m_b}f^{i-1}_{m_am_b}(m_a)\sqrt{2-(m_a-1)m_a}$$
$$+f^{*i-1}_{m_am_b-1}f^{i-1}_{m_am_b}(m_b)\sqrt{2-(m_b-1)m_b})(f^{i}_{n_a-1n_b}(n_a-1)\sqrt{2-(n_a-1)n_a}+f^{i}_{n_an_b-1}(n_b-1)\sqrt{2-(n_b-1)n_b})\Big]$$
$$\frac{1}{4}\Big[(f^{i}_{n_a-2n_b}\sqrt{2-(n_a-2)(n_a-1)}\sqrt{2-(n_a-1)n_a}+f^{i}_{n_an_b-2}\sqrt{2-(n_b-2)(n_b-1)}\sqrt{2-(n_b-1)n_b})$$
$$(f^{*i+1}_{m_a-2m_b}f^{i+1}_{m_am_b}\sqrt{2-(m_a-1)(m_a-2)}\sqrt{2-m_a(m_a-1)}+f^{*i+1}_{m_am_b-2}f^{i+1}_{m_am_b}\sqrt{2-(m_b-1)(m_b-2)}\sqrt{2-m_b(m_b-1)})$$
$$+(f^{*i-1}_{m_a+2m_b}f^{i-1}_{m_am_b}\sqrt{2-(m_a+1)(m_a+2)}\sqrt{2-m_a(m_a+1)}+f^{*i-1}_{m_am_b+2}f^{i-1}_{m_am_b}\sqrt{2-(m_b+1)(m_b+2)}\sqrt{2-m_b(m_b+1)})$$
$$(f^{i}_{n_a+2n_b}\sqrt{2-(n_a+2)(n_a+1)}\sqrt{2-(n_a+1)n_a}+f^{i}_{n_an_b+2}\sqrt{2-(n_b+2)(n_b+1)}\sqrt{2-(n_b+1)n_b})\Big]$$
$$\frac{1}{4}\Big[(f^{i}_{n_a+2n_b}\sqrt{2-(n_a+2)(n_a+1)}\sqrt{2-(n_a+1)n_a}+f^{i}_{n_an_b+2}\sqrt{2-(n_b+2)(n_b+1)}\sqrt{2-(n_b+1)n_b})$$
$$(f^{*i+1}_{m_a+2m_b}f^{i+1}_{m_am_b}\sqrt{2-(m_a+1)(m_a+2)}\sqrt{2-m_a(m_a+1)}+f^{*i+1}_{m_am_b+2}f^{i+1}_{m_am_b}\sqrt{2-(m_b+1)(m_b+2)}\sqrt{2-m_b(m_b+1)})$$
$$+(f^{*i-1}_{m_a-2m_b}f^{i-1}_{m_am_b}\sqrt{2-(m_a-1)(m_a-2)}\sqrt{2-m_a(m_a-1)}+f^{*i-1}_{m_am_b-2}f^{i-1}_{m_am_b}\sqrt{2-(m_b-1)(m_b-2)}\sqrt{2-m_b(m_b-1)})$$
$$(f^{i}_{n_a-2n_b}\sqrt{2-(n_a-2)(n_a-1)}\sqrt{2-(n_a-1)n_a}+f^{i}_{n_an_b-2}\sqrt{2-(n_b-2)(n_b-1)}\sqrt{2-(n_b-1)n_b})\Big]$$
$$\frac{1}{4}\Big[(f^{i}_{n_an_b}\sqrt{2-n_a(n_a+1)}^{2}+f^{i}_{n_an_b}\sqrt{2-n_b(n_b+1)}^{2})\cdot(|f^{i+1}_{m_am_b}|^2\sqrt{2-m_a(m_a-1)}^{2})+|f^{i+1}_{m_am_b}|^2\sqrt{2-m_a(m_a-1)}^{2})$$
$$+(|f^{i-1}_{m_am_b}|^2\sqrt{2-m_a(m_a+1)}^{2}+|f^{i-1}_{m_am_b}|^2\sqrt{2-m_b(m_b+1)}^{2})(f^{i}_{n_an_b}\sqrt{2-n_a(n_a-1)}^{2}+f^{i}_{n_an_b}\sqrt{2-n_b(n_b-1)}^{2})\Big]$$
$$\frac{1}{4}\Big[(f^{i}_{n_an_b}\sqrt{2-n_a(n_a-1)}^{2}+f^{i}_{n_an_b}\sqrt{2-n_b(n_b-1)}^{2})\cdot(|f^{i+1}_{m_am_b}|^2\sqrt{2-m_a(m_a+1)}^{2})+|f^{i+1}_{m_am_b}|^2\sqrt{2-m_a(m_a+1)}^{2})$$
$$+(|f^{i-1}_{m_am_b}|^2\sqrt{2-m_a(m_a+1)}^{2}+|f^{i-1}_{m_am_b}|^2\sqrt{2-m_b(m_b+1)}^{2})(f^{i}_{n_an_b}\sqrt{2-n_a(n_a+1)}^{2}+f^{i}_{n_an_b}\sqrt{2-n_b(n_b+1)}^{2})\Big]\Big]$$

References

[1] Mike H Anderson, Jason R Ensher, Michael R Matthews, Carl E Wieman, and Eric A Cornell. Observation of bose-einstein condensation in a dilute atomic vapor. *science*, 269(5221):198–201, 1995.

[2] Wolfgang Ketterle. Nobel lecture: When atoms behave as waves: Bose-einstein condensation and the atom laser. *Reviews of Modern Physics*, 74(4):1131, 2002.

[3] Maciej Lewenstein, Anna Sanpera, Veronica Ahufinger, Bogdan Damski, Aditi Sen, and Ujjwal Sen. Ultracold atomic gases in optical lattices: mimicking condensed matter physics and beyond. *Advances in Physics*, 56(2):243–379, 2007.

[4] P Bouyer and MA Kasevich. Heisenberg-limited spectroscopy with degenerate bose-einstein gases. *Physical Review A*, 56(2):R1083, 1997.

[5] Stefan Wildermuth, S Hofferberth, Igor Lesanovsky, Steffen Groth, Peter Krüger, Jörg Schmiedmayer, and Israel Bar-Joseph. Sensing electric and magnetic fields with bose-einstein condensates. *Applied physics letters*, 88(26), 2006.

[6] Paul R Berman. *Atom interferometry*. Academic press, 1997.

[7] S Peil, James V Porto, B Laburthe Tolra, JM Obrecht, BE King, M Subbotin, SL Rolston, and William D Phillips. Patterned loading of a bose-einstein condensate into an optical lattice. *Physical Review A*, 67(5):051603, 2003.

[8] Ana Maria Rey. *Ultracold bosonic atoms in optical lattices*. University of Maryland, College Park, 2004.

[9] William D Phillips and Harold Metcalf. Laser deceleration of an atomic beam. *Physical Review Letters*, 48(9):596, 1982.

[10] Iulia M Georgescu, Sahel Ashhab, and Franco Nori. Quantum simulation. *Reviews of Modern Physics*, 86(1):153, 2014.

[11] Andreas Hemmerich. Cooling and trapping neutral atoms with laser light. In *Laser Sources and Applications*, pages 447–473. CRC Press, 2020.

[12] Gilbert Grynberg and Cécile Robilliard. Cold atoms in dissipative optical lattices. *Physics Reports*, 355(5-6):335–451, 2001.

[13] Walter Hofstetter, J Ignacio Cirac, Peter Zoller, Eugene Demler, and MD Lukin. High-temperature superfluidity of fermionic atoms in optical lattices. *Physical review letters*, 89(22): 220407, 2002.

[14] Markus Greiner, Olaf Mandel, Tilman Esslinger, Theodor W Hänsch, and Immanuel Bloch. Quantum phase transition from a superfluid to a mott insulator in a gas of ultracold atoms. *nature*, 415(6867):39–44, 2002.

[15] Nucl Papanicolaou. Unusual phases in quantum spin-1 systems. *Nuclear Physics B*, 305(3): 367–395, 1988.

[16] MS Bulakhov, AS Peletminskii, SV Peletminskii, and Yu V Slyusarenko. Magnetic phases and phase diagram of spin-1 condensate with quadrupole degrees of freedom. *Journal of Physics A: Mathematical and Theoretical*, 54(16):165001, 2021.

[17] Karlo Penc and Andreas M Läuchli. Spin nematic phases in quantum spin systems. In *Introduction to frustrated magnetism: materials, experiments, theory*, pages 331–362. Springer, 2010.

[18] Subir Sachdev. Quantum phase transitions. *Physics world*, 12(4):33, 1999.

[19] Assa Auerbach. *Interacting electrons and quantum magnetism*. Springer Science & Business Media, 2012.

[20] Jonathan Simon, Waseem S Bakr, Ruichao Ma, M Eric Tai, Philipp M Preiss, and Markus Greiner. Quantum simulation of antiferromagnetic spin chains in an optical lattice. *Nature*, 472(7343): 307–312, 2011.

[21] Werner Krauth, Michel Caffarel, and Jean-Philippe Bouchaud. Gutzwiller wave function for a model of strongly interacting bosons. *Physical Review B*, 45(6):3137, 1992.

[22] Jens Eisert, Marcus Cramer, and Martin B Plenio. Area laws for the entanglement entropy-a review. *arXiv preprint arXiv:0808.3773*, 2008.

[23] Guifré Vidal. Efficient simulation of one-dimensional quantum many-body systems. *Physical review letters*, 93(4):040502, 2004.

[24] Frank Verstraete, Juan J Garcia-Ripoll, and Juan Ignacio Cirac. Matrix product density operators: Simulation of finite-temperature and dissipative systems. *Physical review letters*, 93(20): 207204, 2004.

[25] Jacob Biamonte and Ville Bergholm. Tensor networks in a nutshell. *arXiv preprint arXiv:1708.00006*, 2017.

[26] Dieter Jaksch and Peter Zoller. The cold atom hubbard toolbox. *Annals of physics*, 315(1):52–79, 2005.

[27] Dieter Jaksch, Christoph Bruder, Juan Ignacio Cirac, Crispin W Gardiner, and Peter Zoller. Cold bosonic atoms in optical lattices. *Physical Review Letters*, 81(15):3108, 1998.

[28] Gregory H Wannier. The structure of electronic excitation levels in insulating crystals. *Physical Review*, 52(3):191, 1937.

[29] Matthew PA Fisher, Peter B Weichman, Geoffrey Grinstein, and Daniel S Fisher. Boson localization and the superfluid-insulator transition. *Physical Review B*, 40(1):546, 1989.

[30] Luigi Amico and Vittorio Penna. Time-dependent mean-field theory of the superfluid-insulator phase transition. *Physical Review B*, 62(2):1224, 2000.

[31] Eric Duchon, Yen Lee Loh, and Nandini Trivedi. Optical lattice emulators: Bose and fermi hubbard models. *arXiv preprint arXiv:1311.0543*, 2013.

[32] Franz Schwabl. *Quantum mechanics*. Springer Science & Business Media, 2013.

[33] Franz Schwabl. *Advanced quantum mechanics*. Springer Science & Business Media, 2008.

[34] LE Sadler, JM Higbie, SR Leslie, M Vengalattore, and DM Stamper-Kurn. Spontaneous symmetry breaking in a quenched ferromagnetic spinor bose–einstein condensate. *Nature*, 443(7109): 312–315, 2006.

[35] Subroto Mukerjee, Cenke Xu, and JE Moore. Topological defects and the superfluid transition of the s= 1 spinor condensate in two dimensions. *Physical review letters*, 97(12):120406, 2006.

[36] Alexei Kolezhuk. Symmetry breaking in low-dimensional s u (n) antiferromagnets. *Physical Review B*, 78(14):144428, 2008.

[37] Gabriele De Chiara, M Lewenstein, and A Sanpera. Bilinear-biquadratic spin-1 chain undergoing quadratic zeeman effect. *Physical Review B*, 84(5):054451, 2011.

[38] Ian Affleck, Tom Kennedy, Elliott H Lieb, and Hal Tasaki. Rigorous results on valence-bond ground states in antiferromagnets. *Condensed Matter Physics and Exactly Soluble Models: Selecta of Elliott H. Lieb*, pages 249–252, 2004.

[39] F Duncan M Haldane. Continuum dynamics of the 1-d heisenberg antiferromagnet: Identification with the o (3) nonlinear sigma model. *Physics letters a*, 93(9):464–468, 1983.

[40] Yang Xian. Exact results of dimerization order parameter in su (n) antiferromagnetic chains. *Physics Letters A*, 183(5-6):437–440, 1993.

[41] AV Chubukov. Spontaneous dimerization in quantum-spin chains. *Physical Review B*, 43(4): 3337, 1991.

[42] Juan J Garcia-Ripoll, Miguel A Martin-Delgado, and J Ignacio Cirac. Implementation of spin hamiltonians in optical lattices. *Physical review letters*, 93(25):250405, 2004.

[43] Andreas Läuchli, Guido Schmid, and Simon Trebst. Spin nematics correlations in bilinear-biquadratic s= 1 spin chains. *Physical Review B*, 74(14):144426, 2006.

[44] K Rodriguez, A Argüelles, AK Kolezhuk, L Santos, and T Vekua. Field-induced phase transitions of repulsive spin-1 bosons in optical lattices. *Physical Review Letters*, 106(10):105302, 2011.

[45] Martin C Gutzwiller. Effect of correlation on the ferromagnetism of transition metals. *Physical Review Letters*, 10(5):159, 1963.

[46] Jörg Bünemann, W Weber, and F Gebhard. Multiband gutzwiller wave functions for general on-site interactions. *Physical Review B*, 57(12):6896, 1998.

[47] Victor M Perez-Garcia, Humberto Michinel, JI Cirac, M Lewenstein, and P Zoller. Dynamics of bose-einstein condensates: Variational solutions of the gross-pitaevskii equations. *Physical Review A*, 56(2):1424, 1997.

[48] Herbert Goldstein. *Classical mechanics*. Pearson Education India, 2011.

[49] VS Popov. Imaginary-time method in quantum mechanics and field theory. *Physics of Atomic Nuclei*, 68:686–708, 2005.

[50] Nicolaas P Landsman and Ch G Van Weert. Real-and imaginary-time field theory at finite temperature and density. *Physics Reports*, 145(3-4):141–249, 1987.

[51] Matt Visser. How to wick rotate generic curved spacetime. *arXiv preprint arXiv:1702.05572*, 2017.

[52] Sam McArdle, Tyson Jones, Suguru Endo, Ying Li, Simon C Benjamin, and Xiao Yuan. Variational ansatz-based quantum simulation of imaginary time evolution. *npj Quantum Information*, 5(1):75, 2019.

[53] Francesco Turro. Quantum imaginary time propagation algorithm for preparing thermal states. *arXiv preprint arXiv:2306.16580*, 2023.

[54] Juan Camilo Rodriguez. Antiferromagnetic properties of spin-1 bosonic gases in optical lattices, 2021.

[55] Jun John Sakurai and Eugene D Commins. Modern quantum mechanics, revised edition, 1995.

[56] Frank Verstraete, Valentin Murg, and J Ignacio Cirac. Matrix product states, projected entangled pair states, and variational renormalization group methods for quantum spin systems. *Advances in physics*, 57(2):143–224, 2008.

[57] Román Orús. A practical introduction to tensor networks: Matrix product states and projected entangled pair states. *Annals of physics*, 349:117–158, 2014.

[58] Markus Hauru et al. Multiscale entanglement renormalisation ansatz. 2013.

[59] Alexander M Dalzell and Fernando GSL Brandão. Locally accurate mps approximations for ground states of one-dimensional gapped local hamiltonians. *Quantum*, 3:187, 2019.

[60] Benedikt Bruognolo, Zhenyue Zhu, Steven R White, and E Miles Stoudenmire. Matrix product state techniques for two-dimensional systems at finite temperature. *arXiv preprint arXiv:1705.05578*, 2017.

[61] Anton S Buyskikh. Dynamics of quantum many-body systems with long-range interactions. 2017.

[62] Seyed Nariman Saadatmand. Frustrated spin systems, an mps approach. 2017.

[63] Daniel Jaschke, Simone Montangero, and Lincoln D Carr. One-dimensional many-body entangled open quantum systems with tensor network methods. *Quantum science and technology*, 4 (1):013001, 2018.

[64] John Von Neumann. *Mathematical foundations of quantum mechanics: New edition*, volume 53. Princeton university press, 2018.

[65] Jens Eisert. Entanglement and tensor network states. *arXiv preprint arXiv:1308.3318*, 2013.

[66] Matthew B Hastings. An area law for one-dimensional quantum systems. *Journal of statistical mechanics: theory and experiment*, 2007(08):P08024, 2007.

[67] Roman Orus and Guifre Vidal. The itebd algorithm beyond unitary evolution. *arXiv preprint arXiv:0711.3960*, 2007.

[68] Guifré Vidal. Classical simulation of infinite-size quantum lattice systems in one spatial dimension. *Physical review letters*, 98(7):070201, 2007.

[69] Masuo Suzuki. Relationship between d-dimensional quantal spin systems and (d+ 1)-dimensional ising systems: Equivalence, critical exponents and systematic approximants of the partition function and spin correlations. *Progress of theoretical physics*, 56(5):1454–1469, 1976.

[70] J. Romberg. Lecture notes in stable reconstruction with the truncated svd, Fall 2016.

[71] Tsuyoshi Okubo. ptns. https://github.com/TsuyoshiOkubo/pTNS, 2018.

[72] John Alejandro Montilla. Spin coherent states and quadrupolar states in the matsubara formalism for spin-1 bosons, 2024.

[73] Diefo Luis Gonzalez Velazco. World-line quantum monte carlo, 2022.

[74] Tamás András TóTH. Quadrupolar ordering in two-dimensional spin-one systems. Technical report, EPFL, 2011.

[75] Per-Olov Löwdin. Studies in perturbation theory: Part i. an elementary iteration-variation procedure for solving the schrödinger equation by partitioning technique. *Journal of Molecular Spectroscopy*, 10(1-6):12–33, 1963.